Mon. Not. R. Astron. Soc. **000**, 1–?? (2012) Printed 14 June 2012 (MN LATEX style file v2.2)

Constraining the variation of fundamental constants at $z \sim 1.3$ using 21-cm absorbers⋆

H. Rahmani[1], R. Srianand[1], N. Gupta[2], P. Petitjean[3], P. Noterdaeme[3] and D. Albornoz Vásquez[3]

[1] *Inter-University Centre for Astronomy and Astrophysics, Post Bag 4, Ganeshkhind, Pune 411 007, India*
[2] *Netherlands Institute for Radio Astronomy (ASTRON), Postbus 2, 7990 AA, Dwingeloo, The Netherlands*
[3] *Université Pierre et Marie Curie, CNRS-UMR7095, Institut d'Astrophysique de Paris, 98bis Boulevard Arago, 75014 Paris, France*

Accepted. Received; in original form

ABSTRACT

We present high resolution optical spectra obtained with the Ultraviolet and Visual Echelle Spectrograph (UVES) at the Very Large Telescope (VLT) and 21-cm absorption spectra obtained with the Giant Metrewave Radio Telescope (GMRT) and the Green Bank Telescope (GBT) of five quasars along the line of sight of which 21-cm absorption systems at $1.17 < z < 1.56$ have been detected previously. We also present milliarcsec scale radio images of these quasars obtained with the Very Large Baseline Array (VLBA). We use the data on four of these systems to constrain the time variation of $x \equiv g_{\rm p}\alpha^2/\mu$ where $g_{\rm p}$ is the proton gyromagnetic factor, α is the fine structure constant, and μ is the proton-to-electron mass ratio. We carefully evaluate the systematic uncertainties in redshift measurements using cross-correlation analysis and repeated Voigt profile fitting. In two cases we also confirm our results by analysing optical spectra obtained with the Keck telescope. We find the weighted and the simple means of $\Delta x/x$ to be respectively $-(0.1 \pm 1.3) \times 10^{-6}$ and $(0.0 \pm 1.5) \times 10^{-6}$ at the mean redshift of $< z >= 1.36$ corresponding to a look back time of ∼9 Gyr. This is the most stringent constraint ever obtained on $\Delta x/x$. If we only use the two systems towards quasars unresolved at milliarcsec scales, we get the simple mean of $\Delta x/x = +(0.2 \pm 1.6) \times 10^{-6}$. Assuming constancy of other constants we get $\Delta\alpha/\alpha = (0.0 \pm 0.8) \times 10^{-6}$ which is a factor of two better than the best constraints obtained so far using the Many Multiplet Method. On the other hand assuming α and $g_{\rm p}$ have not varied we derive $\Delta\mu/\mu = (0.0 \pm 1.5) \times 10^{-6}$ which is again the best limit ever obtained on the variation of μ over this redshift range. Using independent constraints on $\Delta\alpha/\alpha$ at $z < 1.8$ and $\Delta\mu/\mu$ at $z \sim 0.7$ available in the literature we get $\Delta g_{\rm p}/g_{\rm p} \leq 3.5 \times 10^{-6} (1\sigma)$.

Key words: galaxies: quasar: absorption line – quasar: individual: J0108−0037 – quasar: individual: J0501−0159 – quasar: individual: J1623+0718 – quasar: individual: J2340−0053 – quasar: individual: J2358−1020

1 INTRODUCTION

Most of the successful physical theories rely on the constancy of a few fundamental quantities such as the fine structure constant, $\alpha = e^2/\hbar c$, the proton-to-electron mass ratio, μ, etc. Some modern theories of high energy physics that try to unify the fundamental interactions predict the variation of these dimensionless fundamental constants over cosmological scales (see Uzan 2003, and references therein for more details). Current laboratory constraints exclude any significant variation of these constants over solar system scales and on geological time scales (see Olive & Skillman 2004; Petrov et al. 2006; Rosenband et al. 2008). It is not observationally/experimentally excluded however that they could vary over cosmological scales. Therefore, constraining time and spatial variations of fundamental constants of physics will have a great impact on understanding the true behavior of the nature.

Savedoff (1956) first pointed out the possibility of using redshifted atomic lines from distant objects to test the evolution of dimensionless physical constants. Initial attempts in this field mainly used the Alkali-Doublet (AD) method to constrain α variation (Savedoff 1956; Bahcall & Schmidt 1967; Wolfe et al. 1976; Levshakov 1994; Varshalovich et al. 1996; Cowie & Songaila

⋆ Based on data obtained with UVES at the Very Large Telescope of the European Southern Observatory (Prgm. ID 082.A-0569A, 085.A-0258A, 66.A-0624A, 68.A-0600A, 072.A-0346A, and 074.B-0358A)

1995; Varshalovich et al. 2000; Murphy et al. 2001; Chand et al. 2005). While the AD method is simple, and least affected by systematics related to ionization and chemical inhomogeneities, the limits achieved on $\Delta\alpha/\alpha \equiv (\alpha_z - \alpha_0)/\alpha_0$ are not usually stringent [1]. The most precise value reported to date using this method being $\Delta\alpha/\alpha = -(0.02 \pm 0.55) \times 10^{-5}$ (Chand et al. 2005) over a redshift range of $1.59 \leq z \leq 2.92$.

Dzuba et al. (1999a,b) and Webb et al. (1999) introduced the Many-Multiplet (MM) method as a generalization of the AD method, in which one correlates different multiplets from different ions simultaneously. Applying this method on a sample of 128 absorbers observed at high spectral resolution with the Keck telescope, Murphy et al. (2003) claimed a detection, $\Delta\alpha/\alpha = -(0.57 \pm 0.10) \times 10^{-5}$, over the redshift range $0.2 \leq z \leq 3.7$. However, this result was not confirmed by Srianand et al. (2004) and Chand et al. (2004) who used higher signal-to-noise ratio (SNR $\sim$ 70 per pixel), high spectral resolution ($R \geq 45000$) UVES/VLT data of 23 Mg II systems detected towards 18 quasars in the redshift range $0.4 \leq z \leq 2.3$ and found $\Delta\alpha/\alpha = (-0.06 \pm 0.06) \times 10^{-5}$. This analysis was criticized by Murphy et al. (2007). However, from the reanalysis of the UVES data, using the Voigt profile fitting code VPFIT[2], Srianand et al. (2007) confirmed the null result albeit with larger error bars (i.e $\Delta\alpha/\alpha = (0.01 \pm 0.15) \times 10^{-5}$). Other analysis using only Fe II transitions in two particularly well suited absorption systems at $z = 1.15$ and $z = 1.84$ failed to confirm any variation in α (Quast et al. 2004; Levshakov et al. 2006; Chand et al. 2006; Levshakov et al. 2007). Recently, Webb et al. (2011) have reported the results of the analysis of 153 systems present in quasar spectra observed with VLT/UVES. They find that α increases with increasing cosmological distance from the Earth. Moreover for $z < 1.8$, they confirm the results by Srianand et al. (2007), $\Delta\alpha/\alpha = -(0.6 \pm 1.6) \times 10^{-6}$. However combining their new VLT measurements with their previous Keck measurements they suggest the possibility for a spatial variation of α and speculate on the existence of an α−dipole. If true, this dipole is very difficult to explain theoretically (Olive et al. 2011). While the MM-method provides improved precision, it is affected by systematics related to ionization, chemical inhomogeneities and isotopic composition. The effects of inhomogeneities can be canceled using a large sample of absorption systems but the effects of isotopic composition will likely to remain an issue.

Most of the existing theories predict that the proton-to-electron mass ratio μ should vary much more than α (for example see Olive et al. 2002; Dent & Fairbairn 2003; Dine et al. 2003, and references therein) though some predicts the reverse (Dent et al. 2008). The variations of μ can be probed using H_2 Lyman and Werner band absorption lines (Varshalovich & Levshakov 1993). H_2 molecules are occasionally detected in high redshift damped Lyman-α systems (Petitjean et al. 2000; Ledoux et al. 2003; Noterdaeme et al. 2008; Srianand et al. 2012) with only a handful of them being suitable for probing the variation of μ. No clear indication of any variation in μ in excess of 1 part in 10^5 is seen in the existing data for $z \geq 2$ (Ivanchik et al. 2005; Reinhold et al. 2006; King et al. 2008; Thompson et al. 2009; Wendt & Molaro 2011; van Weerdenburg et al. 2011). By comparing inversion line transitions of NH_3 with the rotational transitions of other molecules, a strong constraint on $\Delta\mu/\mu$ can be obtained (Murphy et al. 2008). At present such an exercise is possible for only two gravitationally lensed systems at $z < 1$ (Henkel et al. 2005, 2008). The best reported constraint is $\Delta\mu/\mu \leq 3.6 \times 10^{-7} (3\sigma)$ at $z = 0.685$ by Kanekar (2011). Detecting more NH_3 absorption towards normal quasars is required to reduce systematics related to the usage of lensed quasars (See Henkel et al. (2008) for discussions on various other systematics).

As the energy of the 21-cm transition is proportional to, $x \equiv \alpha^2 g_p/\mu$, high resolution optical spectra and 21-cm spectra can be used together to probe the combined variation of these constants (Wolfe et al. 1976). Constraints of the order of $\sigma(\Delta x/x) \lesssim 10^{-5}$ were obtained towards individual systems (Cowie & Songaila 1995; Kanekar et al. 2006; Srianand et al. 2010). Tzanavaris et al. (2007) derived $\Delta x/x = (0.63 \pm 0.99) \times 10^{-5}$ for a sample of nine 21-cm absorbers with $0.23 < z < 2.35$. The majority of the 21-cm spectra used in this study were digitally scanned from the printed literature and the UV-optical data were obtained mainly with VLT/UVES. Better constraints can be derived from higher quality spectra in the radio and optical wavelength ranges of a well selected sample of 21-cm absorbers. This is possible now thanks to systematic surveys for 21-cm absorption towards strong Mg II absorbers (e.g. Gupta et al. 2009). This work has resulted in the detection of 9 new 21-cm absorption systems over a narrow redshift range (i.e $1.05 \leq z \leq 1.45$) that can be used for constraining $\Delta x/x$.

While this technique is very powerful there are two issues that introduce systematic uncertainties in the measurements. These are: (i) the identification of the optical component corresponding to the gas that produces the 21-cm absorption and (ii) the fact that the radio and optical sources could probe different volumes of the absorbing gas as the radio emitting region in quasars is in general extended compared to the UV emitting region. It has been suggested that the gas detected by their C I and/or H_2 absorption is closely associated with the 21-cm gas (Cowie & Songaila 1995; Srianand et al. 2010). However, only few 21-cm absorbers show detectable C I and H_2 absorption and even in these cases velocity offsets up to 1-2 km s^{-1} are noticed (Srianand et al. 2012). All these indicate C I/H_2 and 21-cm absorption need not originate from the same physical region. Another option is to connect 21-cm absorption to absorption from singly ionized species that trace H I gas. For example Tzanavaris et al. (2007) have associated the pixel with strongest absorption in the UV with the pixel with the strongest 21-cm absorption. As neighboring pixels are correlated in optical spectra, the redshift of the strongest metal absorption component will be better defined by using simultaneous Voigt profile fits to the absorption lines. This is the method we adopt in the analysis presented here. The second uncertainty discussed above can be minimized by selecting absorbers towards quasars that are compact at milliarcsec scales. While individual measurements may not be completely free of these systematics, even after careful consideration of the specific properties of the system, it should be possible to minimize them and get a statistically reliable measurement using large sample of absorbers.

As different methods used for constraining the fundamental constants suffer from different systematic effects it is important to increase the number of measurements based on each method to address the time and space variation of different constants. Here we provide new measurements of $\Delta x/x$ using a new sample of 21-cm absorbers.

We have selected 5 systems from the literature [4 from Gupta et al. (2009) and one from Kanekar et al. (2009)] previously known to be associated with narrow 21-cm absorption lines towards radio sources that are compact at arcsecond scales. We have ob-

[1] Here α_z and α_0 are the measured values of α at any redshift, z, and in the laboratory on Earth

[2] http://www.ast.cam.ac.uk/ rfc/vpfit.html

Table 1. Log of the optical spectroscopic observation with VLT/UVES

Source name	Exposure name	Date	Starting Time (UT)	Exposure (sec)	Setting	Seeing (arcsec)	Airmass
(1)	(2)	(3)	(4)	(5)	(6)	(7)	(8)
J0108−0037	EXP1	2008-11-21	01:15:02	3700	390+580	0.64	1.11
	EXP2	2008-11-23	02:41:45	3700	390+580	0.77	1.13
	EXP3	2008-11-25	01:52:08	3700	390+580	0.89	1.10
	EXP4	2008-12-03	01:11:20	3690	390+580	0.71	1.10
J1623+0718	EXP1	2010-05-08	05:48:49	3340	390+580	1.33	1.18
	EXP2	2010-08-07	01:08:41	3340	390+580	0.82	1.23
	EXP3	2010-08-08	00:45:37	3340	390+580	0.86	1.20
	EXP4	2010-08-09	00:56:50	3340	390+580	0.70	1.22
J2340−0053	EXP1	2008-10-02	02:39:30	4500	390+580	0.88	1.13
	EXP2	2008-10-05	02:01:02	4500	390+580	0.82	1.17
	EXP3	2008-10-05	03:25:10	4500	390+580	0.88	1.09
	EXP4	2008-10-06	00:28:59	4500	390+580	0.90	1.50
	EXP5	2008-10-06	01:55:32	4500	390+580	0.79	1.18
	EXP6	2008-10-28	04:41:03	4500	390+580	0.79	1.45
J2358−1020	EXP1	2010-08-04	06:27:07	3340	390+580	0.75	1.10
	EXP2	2010-08-06	04:43:45	3340	390+580	0.69	1.40
	EXP3	2010-08-06	05:50:01	3340	390+580	0.71	1.16
	EXP4	2010-08-06	06:55:07	3340	390+580	0.64	1.05
	EXP5	2010-08-06	08:00:14	3340	390+580	0.65	1.04
	EXP6	2010-08-06	09:05:21	3340	390+580	0.77	1.10
	EXP7	2010-08-07	04:53:34	3340	390+580	0.78	1.34
J0501−0159	EXP1	2000-10-21	06:13:17	3600	437+750	0.61	1.17
	EXP2	2000-10-23	04:08:46	3600	346+580	0.53	1.73
	EXP3	2001-10-16	07:20:51	5400	346+570	0.46	1.10
	EXP4	2004-10-21	04:38:08	4500	390+564	0.63	1.25
	EXP5	2004-10-21	05:42:38	5400	390+564	0.79	1.56
	EXP6	2004-10-21	07:05:51	3600	437+860	1.17	1.10
	EXP7	2004-10-22	04:38:08	3600	437+860	0.84	1.29
	EXP8	2004-10-22	05:42:42	4500	390+564	0.89	1.12
	EXP9	2004-10-22	07:05:55	4500	390+564	0.59	1.81
	EXP10	2004-10-22	08:04:58	3360	437+860	1.00	1.09

Column 1: Source name; Column 2: Assigned name for the exposure. Column 3: Date of observation; Column 4: Starting time of exposure; Column 5: Exposure time; Column 6: Spectrograph settings; Column 7: Seeing in arcsec; Column 8: Airmass at the beginning of the exposures.

tained high resolution UV and radio data of the quasars together with high resolution Very Large Baseline Array (VLBA) images. We report here the analysis of this dataset. This paper is organized as following. In Section 2, we present details of optical and radio observations and data reduction. In Sections 3 and 4 we provide details of Gaussian fits to the 21-cm absorption lines and Voigt profile fitting of the UV lines. In Section 5, we summarize our $\Delta x/x$ measurements in individual systems and discuss the associated systematic errors. In Section 6 we discuss the results and conclude. We use simultaneous Voigt profile fits to identify the redshift of the strongest UV component closest to the 21-cm absorption. We also discuss the results if we adopt the method used by Tzanavaris et al. (2007).

2 OBSERVATIONS AND DATA REDUCTION

2.1 Optical spectroscopy

The optical spectroscopic observations of quasars were carried out with UVES (Dekker et al. 2000) at the VLT UT2 8.2-m telescope at Paranal (Chile) in service mode [Programs 082.A-0569A and 085.A-0258A]. All observations were performed using the standard beam splitter with the dichroic #2 (setting 390+580) that covers roughly from 330 to 450 nm on the BLUE CCD and from 465 to 578 nm and 583 to 680 nm on the two RED CCDs. Slit width of 1 arcsec and CCD readout with 2x2 binning were used for all the observations resulting in a pixel size of ≈ 1.7 km s^{-1} and spectral resolution of ≈45000. D'Odorico et al. (2000) have shown that the resetting of the grating between an object exposure and the ThAr calibration lamp exposure can result in an error of the order of a few hundred meters per second in the wavelength calibration. To minimize this effect each science exposure was followed immediately by an attached set of 5 ThAr lamp exposures. In the case of J0501−0159 we have retrieved all the UVES data available in the ESO archive. As these spectra were not acquired specifically for constraining the variation of fundamental constants there is no attached calibration lamp exposure taken along with the science observations. However this data were reduced using the available lamp spectra closest in time.

The data were reduced with the UVES Common Pipeline Library (CPL) data reduction pipeline release 4.7.8[3] using the optimal extraction method. We used 4$^{\rm th}$ order polynomials to find the dispersion solution. The number of suitable ThAr lines used for wavelength calibration was always larger than 400 and the rms error was found to be in the range 70 – 80 m s^{-1} with zero average. However, this error applies only to regions very close to the ThAr emission

[3] http://www.eso.org/sci/facilities/paranal/instruments/uves/doc/

lines that are used to compute the wavelength solution. In principle the calibration error in the regions in between ThAr emission line can be typically of the order of a few hundred meters per second (for example see Agafonova et al. 2011).

All the spectra were corrected for the motion of the observatory around the barycenter of the Sun-Earth system. The velocity component of the observatory's barycentric motion towards the line of sight to the object was calculated at the exposure mid point (see Table 1). Conversion of air to vacuum wavelengths was performed using the formula given in Edlén (1966). For the co-addition of the different exposures, we interpolated the individual spectra and their errors to a common wavelength array and then computed the weighted mean using weights estimated from the errors in each pixel. In order to fit the continuum we considered only specific regions (20-100 Å) around the absorption lines of interest and fitted the points without any absorption with a lower order cubic spline.

Voigt profile fits of the absorptions from different species have been performed using VPFIT, version 9.5. While simultaneously fitting absorption profiles of a system, we assumed that all the singly ionized species (e.g. Fe II, Si II, Zn II, etc.) are kinematically associated with the same gas. We also assumed the velocity broadening is predominantly turbulent. Therefore, we used the same z and b parameters for a given component for all the species. The error on the redshift of individual Voigt profile components depends on the statistical error from the fitting procedure and the systematic errors related to the procedure itself and the wavelength calibration. The VPFIT program estimates errors using only the diagonal terms of the covariance matrix. Although the reliability of the errors have been confirmed for unblended components (see King et al. 2009; Carswell et al. 2011), errors from VPFIT are underestimated in the case of blended components. To account for this and other systematic errors discussed above, we perform Voigt profile fits for a given system several times (see Section 2.1.3 for details). In Table 2 we summarize the laboratory wavelengths and oscillator strengths of all transitions that are used in this study. In this table we also give a short name (id) to specific transitions for future reference in the text.

Table 2. Adopted atomic data for different species used in this study

Species	id	wavelength (Å)	Ref	oscillator† strength
Si II	a	1808.01288	[2]	0.00208
Cr II	b1	2056.25682	[2]	0.1030
Cr II	b2	2062.23594	[2]	0.0759
Cr II	b3	2066.16391	[2]	0.0512
Mn II	c1	2576.87534	[2]	0.361
Mn II	c2	2594.49669	[2]	0.280
Mn II	c3	2606.45883	[2]	0.198
Fe II	d1	1608.45081	[3]	0.0577
Fe II	d2	1611.2005	[1]	0.00138
Fe II	d3	2249.8768	[1]	0.00182
Fe II	d4	2260.77934	[2]	0.00244
Fe II	d5	2344.21282	[2]	0.114
Fe II	d6	2374.46013	[2]	0.0313
Fe II	d7	2382.76411	[2]	0.320
Fe II	d8	2586.64937	[2]	0.0691
Fe II	d9	2600.17223	[2]	0.239
Ni II	e1	1454.842	[1]	0.0276
Ni II	e2	1467.259	[1]	0.0063
Ni II	e3	1467.756	[1]	0.0099
Ni II	e4	1502.148	[1]	0.006
Ni II	e5	1703.4119	[1]	0.006
Ni II	e6	1709.6042	[1]	0.0324
Ni II	e7	1741.5531	[1]	0.0427
Ni II	e8	1751.9157	[1]	0.0277
Zn II	f1	2026.13695	[2]	0.501
Zn II	f2	2062.66028	[2]	0.246
C I	g1	1560.3092	[1]	0.0774
C I	g2	1656.9284	[1]	0.149
Mg I	h1	2026.47504	[2]	0.113
Mg I	h2	2852.96282	[2]	1.83

References. [1] – Morton (2003); [2] – Aldenius (2009); [3] – Nave & Sansonetti (2011)
† Oscillator strengths are from Morton (2003) apart from the Ni IIλ1454 where we use the value from Zsargo & Federman (1998) that provide best fit to our data while being consistent within error to the values given in Morton (2003).

2.1.1 *Systematic errors in wavelength calibration*

The shortcomings of the ThAr wavelength calibration of quasars spectra taken with VLT/UVES has already been discussed by number of authors (Chand et al. 2006; Levshakov et al. 2006; Molaro et al. 2008; Thompson et al. 2009; Whitmore et al. 2010; Agafonova et al. 2011). Overall velocity shifts of the order of a few hundred meters per second have been observed between the spectra of the same object calibrated with an iodine cell spectrum or with a ThAr calibration lamp (Whitmore et al. 2010). The latter authors have also shown that intra-order velocity shifts of more than 200 m s^{-1} are present within a given exposure. Therefore, while we have taken enough care during the data reduction, wavelength uncertainties due to these systematics still remain. We therefore performed several tests to estimate these systematic effects.

2.1.2 *Cross-correlation analysis*

We cross-correlate individual spectra (in a window comprising of the absorption lines associated with the systems of interest) with the combined spectrum to estimate the velocity offset between them. For this we first rebin each pixel (δv~2.0 km s^{-1}) to 25 sub-pixels with a velocity width of ~80 m s^{-1}. This rebinning is done by interpolating the spectrum with a polynomial using Neville algorithm

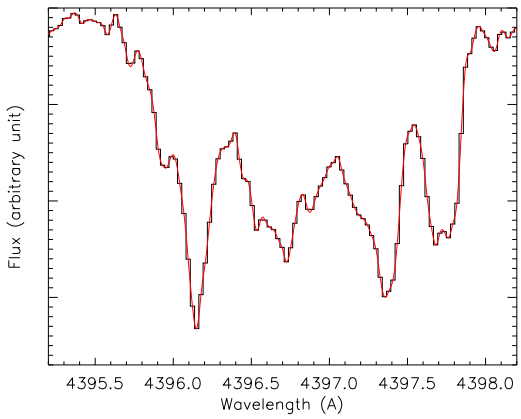

Figure 1. Example of the interpolation of a spectrum using Neville's algorithm. The histogram curve is an absorption profile and the smooth curve gives the interpolated spectrum achieved using Neville's algorithm.

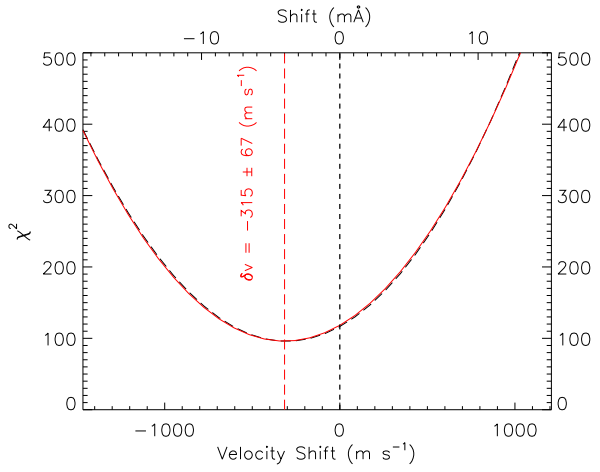

Figure 2. Velocity shift between the combined spectra and one of the exposures for the Fe II λ1608 absorption profile in J2340−0057. The dashed curve shows the χ^2 (see 2.1.1) as a function of the applied velocity shift and the continuous curve is the best fitted parabola. The short and long dashed vertical lines respectively mark the zero velocity and velocity of −315 m s^{-1} at which the χ^2 is minimum.

(see Fig. 1). For finding the relative shift between the combined spectrum I and the spectrum I_i of the i'th exposure, we proceed as follows: we fix I and shift I_i relative to I by steps of 0.04 times the original pixel size (i.e 80 m s^{-1}). At each step characterized by the shift $\delta\lambda$, a χ^2 is calculated from the difference in fluxes between I and I_i and the flux error of I_i: $\chi^2(\delta\lambda) = \Sigma_j[I_j - I_{i,j}(\delta\lambda)]^2/\sigma^2_{i,j}(\delta\lambda)$, where $I_{i,j}$ is the normalized flux of the j'th pixel of the i'th exposure with the error $\sigma_{i,j}$. This χ^2 is a function of $\delta\lambda$ and is minimum when the two profiles are aligned. We fit the function $\chi^2(\delta\lambda)$ with a parabola and the value of $\delta\lambda_{min}$ at which the χ^2 is minimum is taken as the wavelength offset between the two absorption profiles (See Fig. 2). Following the standard statistical procedure we assign 1σ errors to this $\delta\lambda_{min}$ by computing the required change in $\delta\lambda$ so that $\Delta\chi^2 = \chi^2 - \chi^2_{min} = 1$. This procedure is similar to that implemented by Agafonova et al. (2011) to find the shift between their spectra but with the difference that they use the simple sum of the square of the differences in fluxes instead of χ^2. Using χ^2 has the advantage that we can associate an error to the measured shift. For each exposure we measure the shifts (of all transitions used in our Voigt profile fitting) along with the errors. Having measured a shift and error for each transition in each exposure we find their weighted mean and weighted standard deviation as an estimate of the systematic error due to a constant shift in the redshift of the absorbing system. In addition, the correlation analysis not only allows us to identify exposures with abnormally large wavelength shifts but also to identify absorption lines that may be affected by calibration uncertainties in one of the exposures. Results of this exercise for four quasars in our sample are summarized in Tables A1, A2, A3, and A4 of the Appendix. It is clear from these tables that individual exposures have typical (rms) shifts of up to ∼350 m s^{-1}.

2.1.3 Repeated Voigt profile fitting analysis

We use simultaneous fitting of several transitions to measure the redshift of a given component and the associated error. To estimate the latter we perform repeated Voigt profile fitting using several combinations of spectra excluding one exposure at a time. This exercise allows us to understand the influence of individual exposures on our final redshift measurement. Similarly using the final combined spectra we perform repeated Voigt profile fitting including and excluding different transitions. This will allow us to estimate the redshift uncertainties due to the choice of lines used in the Voigt profile fitting and also the random intra-order shifts.

It is known that the wavelength calibration is most accurate in regions close to the ThAr emission lines that are used to derive the pixel to wavelength solution (see Agafonova et al. 2011). Therefore, we performed Voigt profile fitting of those transitions that have at least one ThAr emission line (that was used for wavelength calibration) within ±50 km s^{-1} from the UV-optical component that coincides with the 21-cm component.

We use the results of the above exercises along with the results of the cross-correlation analysis to quantify the final errors in the redshift measurements.

2.2 Archival Keck/HIRES spectrum

For two quasars studied here (J2340−0053 and J0501−0159) high resolution echelle spectra were obtained with Keck/HIRES by Prof. Prochaska and collaborators as part of their database archive for abundance studies in DLAs (Prochaska et al. 2001, 2007). The wavelength coverage in both cases is less than that of our VLT/UVES spectra. The spectral resolution of the J2340−0053 Keck/HIRES spectrum is roughly the same as our VLT/UVES spectrum (i.e 6.0 km s^{-1}) but its SNR is less than ours. In the case of J0501−0159 the spectral resolution of Keck/HIRES is ∼ 8.0 km s^{-1} and both spectra have comparable SNR. We fit the absorption profiles in the Keck/HIRES in order to compare the results obtained with the two telescopes. This exercise helps us to understand the systematic errors in the wavelength calibration and especially the existence of any global shift between the two spectra.

2.3 GMRT observations and morphology of the background sources

Gupta et al. (2009) used a bandwidth of 1 MHz split into 128 frequency channels in the course of their GMRT survey for 21-cm absorption in strong Mg II absorbers. This yields a velocity resolution of ∼4 km s^{-1} per channel. In our new GMRT observations for three sources (J0108−0038, J2340−0053, and J2385−1020) we have used a band width of 0.25 MHz split into 128 channels yielding a channel resolution of ∼1 km s^{-1}. To increase the spectral SNR, each object was observed for 24 to 30 hrs (i.e in three full synthesis observations). In the case of J1623+0718 a bandwidth of 0.5 MHz was used to adequately cover both the 21-cm components. Spectral resolution in this case is ∼ 2 km s^{-1}.

The data were acquired in the two orthogonal polarization channels RR and LL. For the flux density/bandpass calibration of GMRT data, standard flux density calibrators were observed for 10-15 min every two hours. A phase calibrator was also observed for 10 min every 45 min to get reliable phase solutions. The GMRT data were reduced using the NRAO AIPS package following the standard procedures. Special care was taken to exclude the baselines and time stamps affected by the radio frequency interference (RFI). The spectra at the quasar positions were extracted from the RR and LL spectral cubes and compared for consistency. If necessary, a first-order cubic-spline was fitted to remove the residual continuum. The two polarization channels were then combined to

Table 3. Shifts (in units of m s^{-1}) between individual 21-cm spectra relative to the combined one for J0108−0037 at the position of 21-cm absorption

LL_1	RR_1	LL_2	RR_2	LL_3	RR_3
47±55	99±96	71±104	-180±133	-178±191	-249±192
weighted mean			+17		
weighted standard deviation			122		

get the stokes I spectrum which was then shifted to the heliocentric frame. We used the AIPS task CVEL to correct the observed data for the Earth's motion and rotation. We obtained the mean spectrum weighting the flux by the inverse rms square in the line free channels.

2.3.1 Redshift uncertainties

We can use the cross-correlation analysis described in Section 2.1.2 to search for any possible frequency off-set between spectra of the same object obtained at different epochs and through different polarization channels. To avoid the effect of poor SNR, we consider here only J0108−0037. We have useful data obtained during three epochs and hence 6 individual spectra to carry out a correlation analysis of individual spectra relative to the final combined one. The results are summarized in Table 3. Here LL_i and RR_i are corresponding to the LL and RR polarizations of the i'th observation of this source. The weighted standard deviation of these observed shifts is 122 m s^{-1} and observed values are up to 249 m s^{-1}. We will thus consider the systematic error in radio frequency calibration to be 122 m s^{-1} or equivalently 0.4×10^{-6} in $\Delta x/x$.

Below, we will give the results of Gaussian fitting of the 21-cm lines using the combined spectrum and spectra obtained through individual polarization channels. The statistical errors in 21-cm redshift determination are found to be much larger than the above quoted systematic shift.

2.3.2 Milliarcsec images of the background sources

The five quasars being studied in this work seem to be compact in FIRST and GMRT 610-MHz images that both have 5 arcsec spatial resolution. VLBA L-band 1422 MHz observations of 4 sources (i.e. excluding J0501−0159) have been obtained as a part of a larger survey of radio sources with damped Lyman-α absorbers (DLAs) and Mg II absorption systems along their line of sight to understand the relationship between radio structure and the detectability of 21-cm absorption (see Srianand et al. 2012; Gupta et al. 2012). Details of observational setups and data reduction can be found in these papers. The final images of these 4 sources are shown in Fig. 3.

In Fig. 3 we see that J0108−0037 is clearly resolved into several components at milliarcsec scales. We note that 73% of the L-band flux density detected in the FIRST image is recovered in our VLBA image with the compact unresolved component having 53% of the flux density. In the 8 GHz VLBA image the strong component seen in our L-band VLBA image gets resolved into two distinct components and only one of them may be associated to the optical continuum emitting region. This makes our task difficult while trying to assign 21-cm absorbers to their UV-optical absorbing counterparts as there is a high probability that additional contribution to the 21-cm absorption may come from gas that is not located along the optical line of sight.

From Fig. 3, we see that the source J1623+0718 is unresolved even at milliarcsec scales. However, the VLBA observation recovers only 42% of the flux density detected in arcsec scale FIRST image. Based on a Gaussian fit to our VLBA image we derive that the maximum angular extent of the compact component is 4.64 mas. This means the size of the radio beam at the redshift of the absorber, $z \sim 1.337$, is less than 39 pc. It is likely that this radio source samples the same region of the absorbing gas as the optical source. High frequency VLBA observations are not available in the literature for this source. In our recent L-band GMRT observations we find that the flux density of this source at arcsec scales is similar to what is seen in the FIRST image. This suggests that the ∼58 % missing flux in our L-band VLBA image may be due to a diffuse extended radio emitting component that might have got resolved out at milliarcsec scale. Therefore if the absorbing gas is extended beyond 39 pc then the absorption against this diffuse component may also contribute to our GMRT spectrum.

The source J2340−0053 is clearly unresolved in our L-band VLBA image. It is also unresolved in the high frequency VLBA images taken at 2 and 8 GHz (for example see Kovalev et al. 2007). The radio flux density shows a peak around 1.4 to 2.3 MHz with a sharp decrease towards low frequency end. All this is consistent with the background quasar being a GHz peaked compact self-absorbed radio source. Using the flux density measurement in the FIRST catalog we find 90% of the L-band flux density in the FIRST image is recovered in the unresolved VLBA component. Gaussian fitting of the L-band VLBA image gives the maximum angular extent of the object to be 1.71 mas. Using the redshift of the 21-cm absorber at $z \sim 1.36$ we estimate the maximum physical size of the quasar radio beam at the position of the absorbing gas to be ≤15 pc. Thus it is most likely that optical and radio beams sample the same volume of absorbing gas. Therefore we expect the systematics related to the structure of the background radio source to be minimum in this case.

The source J2358−1020, observed with a resolution of ∼20 mas (Fig. 3), is unresolved in our L-band VLBA image. This source remains unresolved even in higher frequency VLBA observations taken at 2 and 8 GHz (Fomalont et al. 2000; Fey & Charlot 2000). Similarly to the case of J2340−0053, this source is a GHz peaked radio source with a clear turnaround at the low frequency end. Moreover, in our VLBA observation we recover 74% of the flux detected in FIRST observation. A single Gaussian component fit represents its 1422 MHz VLBA image well. The largest angular size of the source is constrained to be ≤3.71 mas which is equal to ≤31 pc at the redshift of the absorbing system. All this suggests that the optical and radio sight lines probe the same volume of the absorbing gas. Therefore we expect the systematics related to the radio structure of this background quasar also be minimum.

The background radio source J0501−0159, also known as PKS 0458−020, exhibits multiple components at arcsecond and milliarcsecond scales. The radio structure of this source is investigated in detail by Briggs et al. (1989) to determine the spatial extent of the $z_{abs} = 2.04$ absorber 21-cm detected by (Wolfe et al. 1985). At 1.6 GHz, the source is resolved into two components that are marginally separated at 1 arcsec resolution (see Fig.1 of Briggs et al. 1989). In the 10 mas resolution map at 608 MHz, the frequency that is also close to the redshifted 21-cm frequency of the $z_{abs} = 1.56$ absorber, the compact 'core' at arcsecond scales is further resolved into a jet and a diffuse component (see Fig.2 of Briggs et al. 1989). The radio emission in these different components is strong enough to contribute to the detected 21-cm absorption. Therefore, if the absorbing gas extends over several milliarcsecs, the possibility of velocity offsets between radio and optical

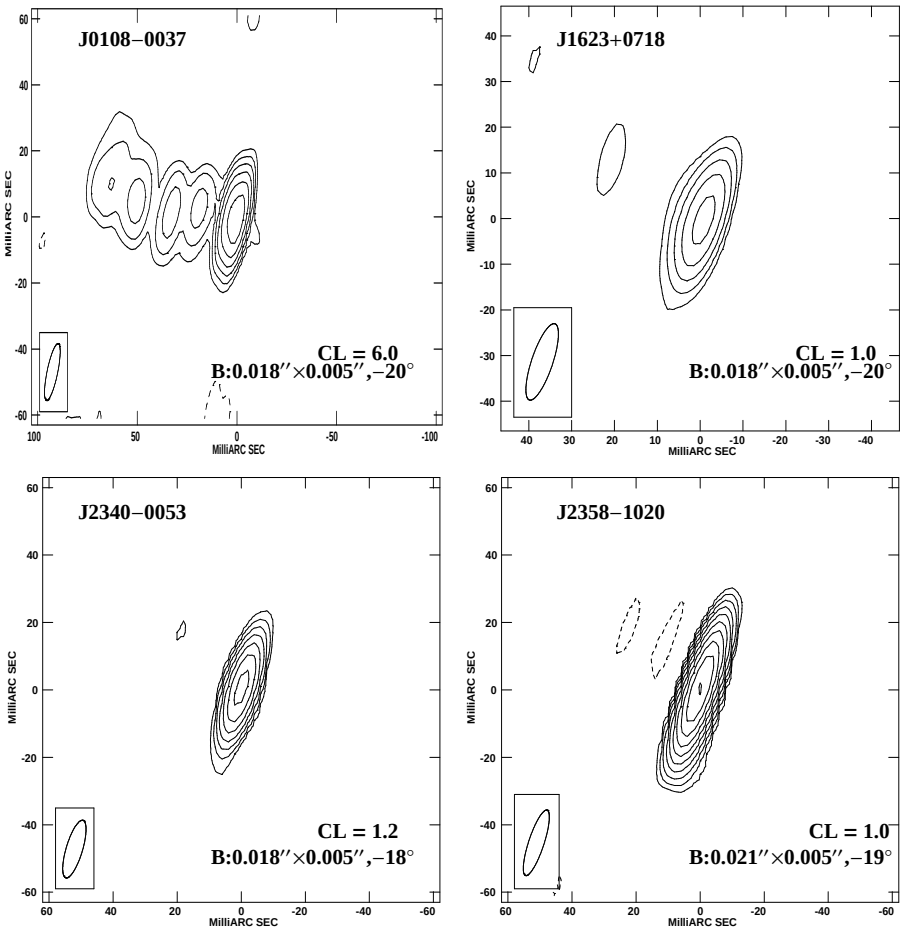

Figure 3. Contour plots of VLBA images at 1.4 GHz. The restoring beam, shown as the ellipse, and the first contour level (CL) in mJy beam^{-1} are provided at the bottom of each image. The contour levels are plotted as CL×(−1, 1, 2, 4, 8,...) mJy beam^{-1}.

absorption lines due to the extended radio structure cannot be ruled out in this case.

3 GAUSSIAN FITS TO 21-CM ABSORPTION LINES

3.1 J0108−0037

Gupta et al. (2007) have reported 21-cm absorption from the $z_{\rm abs}$ = 1.371 Mg II system towards J0108−0037. Despite a low rest equivalent width of ∼0.3 Å for the Mg II doublet, other absorption lines of weaker metal transitions are clearly seen even in the SDSS spectrum. Note that $z_{\rm abs}$ is very close to $z_{\rm em}$ with an apparent ejection velocity of only ∼180 km s^{-1}. The 21-cm absorption is well approximated by a single Gaussian component in the GMRT data with a resolution of 4 km s^{-1}channel^{-1}. Subsequently, we observed this system for 25 hours spread over three observing runs of similar durations to obtain a spectrum with 1 km s^{-1} channel width. The final 21-cm absorption spectrum is the inverse-variance weighted mean of these 3 spectra (see top panel in Fig. 4). It can be seen from the figure that the absorption profile is smooth and that more than one Gaussian component is required to fit the profile. The smooth broad wing could indicate either a shallow component with a large velocity width or a blend of several weak narrow components as suggested by the fit to metal absorption lines (see section 4.1). We find that at least three components are needed to obtain a good fit with a reduced χ^2 of 1.1. The result of this fit is over-plotted on top of the observed spectrum in Fig. 4. The redshift of the strongest 21-cm component is 1.3709710(11) (see Table 4). The reduced χ^2 is 1.03 for a 4 component fit. This suggests that four components are adequate to represent the 21-cm profile. The redshift of the strongest 21-cm component in this case is 1.3709694(53).

3.2 J0501−0159

The sight line towards this quasar is interesting as it covers two 21-cm absorbers at z = 2.04 and 1.56 (Wolfe et al. 1985; Kanekar et al. 2009). Kanekar et al. (2010) fitted the 21-cm absorption with a single component at z_{21} = 1.5605300(25) in a spectrum smoothed to a resolution of 1.3 km s^{-1}channel^{-1}. Using the pipeline based on the NRAO's GBTIDL package we re-reduced their archived GBT data. Details on the GBT data reduction can be found in Srianand et al. (2012). The original data was obtained with two sets of spectral resolutions (i.e. 0.33 and 0.66 km s^{-1} channel^{-1}). However, we rebinned the individual spectra to 1.3 km s^{-1} channel^{-1} resolution before combining them. This is done to match the resolution to our GMRT spectra of other sources. The absorption profile of this 21-cm absorber (shown in the top panel of Fig. 4) shows the existence of two absorbing components. Redshifts obtained from the

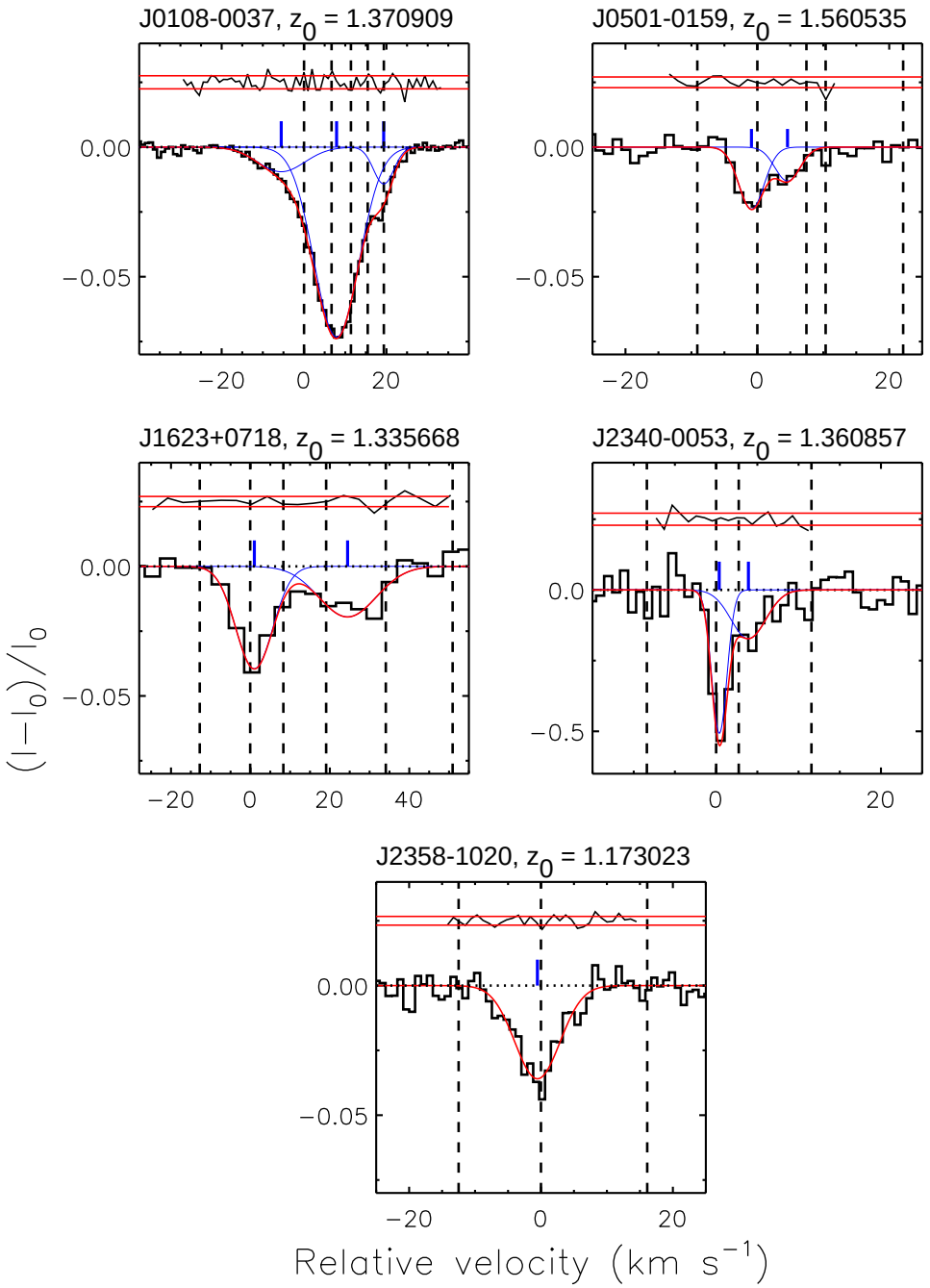

Figure 4. 21-cm absorption profiles of all the Mg II absorbers in our sample. The redshift used to define the zero velocity scale is given in each panel as z_0. The ticks mark the positions of the 21-cm absorption components. The long-dashed vertical lines are the positions of UV-optical absorber components (see Section 4). The normalized residuals (i.e. ([data]−[model]) / [error]) for each fit is shown in the top of each panel along with the 1σ horizontal line.

two components fit are summarized in Table 4. It can be seen that the spectra obtained in two polarization channels give consistent redshifts for the two components within measurement uncertainties (i.e 380 and 700 m s^{-1} for the strong and the weak component respectively).

3.3 J1623+0718

The 21-cm absorption at $z \sim 1.336$ towards J1623+0718 was first reported by Gupta et al. (2009) with two components. Using their spectrum we measure z_{21} = 1.3356755(53) and 1.3358518(108). As the background source as well as the absorption lines are weak we reobserved this system for 16.8 hours spread over two full synthesis with a channel width of 2 km s^{-1}. Unfortunately the SNR in the final spectrum is not high enough to provide accurate red-

Table 4. Results of multi-component Gaussian fits to the 21-cm absorption line

Quasar	Channel width	z_{21}	δv	δv_{RR}	δv_{LL}
(1)	(2)	(3)	(4)	(5)	(6)
J0108−0037	1	1.3708647(115)	1.45	....	....
		1.3709710(11)	0.14	....	....
		1.3710614(19)	0.24	....	....
J0501−0159	1	1.5605277(32)†	0.38	$-0.12 \pm 0.16^{\star}$	$+0.30 \pm 0.44^{\star\star}$
	1	1.5605745(60)	0.70	$+0.46 \pm 0.67^{\star}$	$-0.16 \pm 0.40^{\star\star}$
J1623+0718	4	1.3356761(51)†	0.65	$+0.14 \pm 1.42$	-0.47 ± 0.78
		1.3358591(98)	1.26	-1.60 ± 3.70	$+0.76 \pm 2.41$
J2340−0053	1	1.3608595(14)†	0.18	$+0.17 \pm 0.20$	$+0.00 \pm 0.19$
		1.3608874(106)	1.35	$+0.42 \pm 0.48$	$+0.39 \pm 2.60$
J2358−1020	1	1.1730206(17)	0.23	$+0.74 \pm 0.51$	-0.55 ± 0.28
		1.1730188(25)†	0.35	$+0.61 \pm 0.48$	-0.30 ± 0.28

Column 1: Source name. Column 2: Channel width in km s^{-1}. Column 3: Absorption redshift and its error. Column 4: The error in the absorption redshift in km s^{-1}. Column 5: Measured velocity offset with respect to the z_{21} given in Column 3 in km s^{-1} when only RR spectrum considered. Column 6: Measured velocity offset in km s^{-1} when only LL spectrum considered.
* XX polarization in GBT; ** YY polarization in GBT
† component and corresponding z_{21} used for measuring $\Delta x/x$

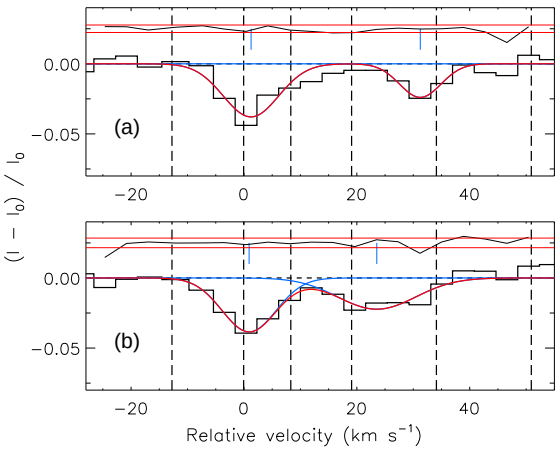

Figure 5. New and old combined 21-cm spectra of J1623+0718 respectively in panel (a) and (b) with the best fitted double Gaussian in each case shown as continuous curve. The thick histogram in the bottom of two panels show the residual of the fits that are shifted by a constant offset for clarity. The $v = 0$ is at $z = 1.335668$. Although the redshift of the first component in both new and old spectra matches very well the redshift of the second component (at $v \sim 35$ km s^{-1}in the top panel) differs by 7.7±2.0 km s^{-1} between the two spectra. The normalized residuals (i.e. ([data]–[model]) / [error]) for each fit is shown in the top of each panel along with the 1σ horizontal line.

shift measurements. Therefore, we rebinned our new spectrum to a resolution of 4 km s^{-1} channel^{-1}. The redshifts of the two components in the new combined spectrum are $z_{21} = 1.3356782(85)$ and 1.3359118(116). While the redshift of the blue component is consistent with the measurement based on the spectrum of Gupta et al. (2009) the redshift of the second component is off by 7.7±2.0 km s^{-1} (see Fig. 5). We attribute this to the low optical depth in this component or to the presence of a low level RFI affecting the shallow feature. Because of this reason we do not use this component to constrain $\Delta x/x$. In order to increase the SNR further, we combined our new spectra with the spectra obtained by Gupta et al. (2009). The Gaussian fit to the combined spectrum is shown in Fig. 4. The fit results are summarized in Table 4. The measured $z_{21} = 1.3356761(51)$ for the main 21-cm component agrees well with the measurements based on spectra obtained in individual polarization channels. The redshift uncertainty in this case corresponds to a velocity of 650 m s^{-1}.

3.4 J2340−0053

The 21-cm absorption at $z = 1.3606$ along the line of sight towards this quasar was discovered by Gupta et al. (2009). We have acquired additional 3x8 hours of GMRT data at 1 km s^{-1} channel^{-1} resolution. However these data are found to be unusable due to RFI. So we use here only the the GMRT 21-cm absorption spectrum with, $\delta v \sim 1$ km s^{-1} channel^{-1}, obtained by Gupta et al. (2009) and shown in Fig. 4. The spectrum clearly shows two absorbing components, the bluer being quite strong. The continuous line in Fig 4 shows the double Gaussian fit to the 21-cm absorption profile. The two components are also shown (see also Table 4). The redshifts of the two components are z=1.3608595(14) and z=1.3608874(106). The redshift errors for the Gaussian fits correspond to uncertainties in the velocity scale of 180 m s^{-1} and 1350 m s^{-1} respectively. The above redshifts are found to be consistent with those obtained by fitting RR and LL spectra separately (see Table 4).

3.5 J2358−1020

The 21-cm absorption along the line of sight towards this quasar was first discovered by Gupta et al. (2007). The 21-cm absorption is well approximated by a single Gaussian component at a spectral resolution of 2 km s^{-1}channel^{-1} (Gupta et al. 2009). Two high resolution spectra of this object with $\delta v \sim 1$ km s^{-1} per channel were acquired during subsequent observations (2×8 hours). The shape

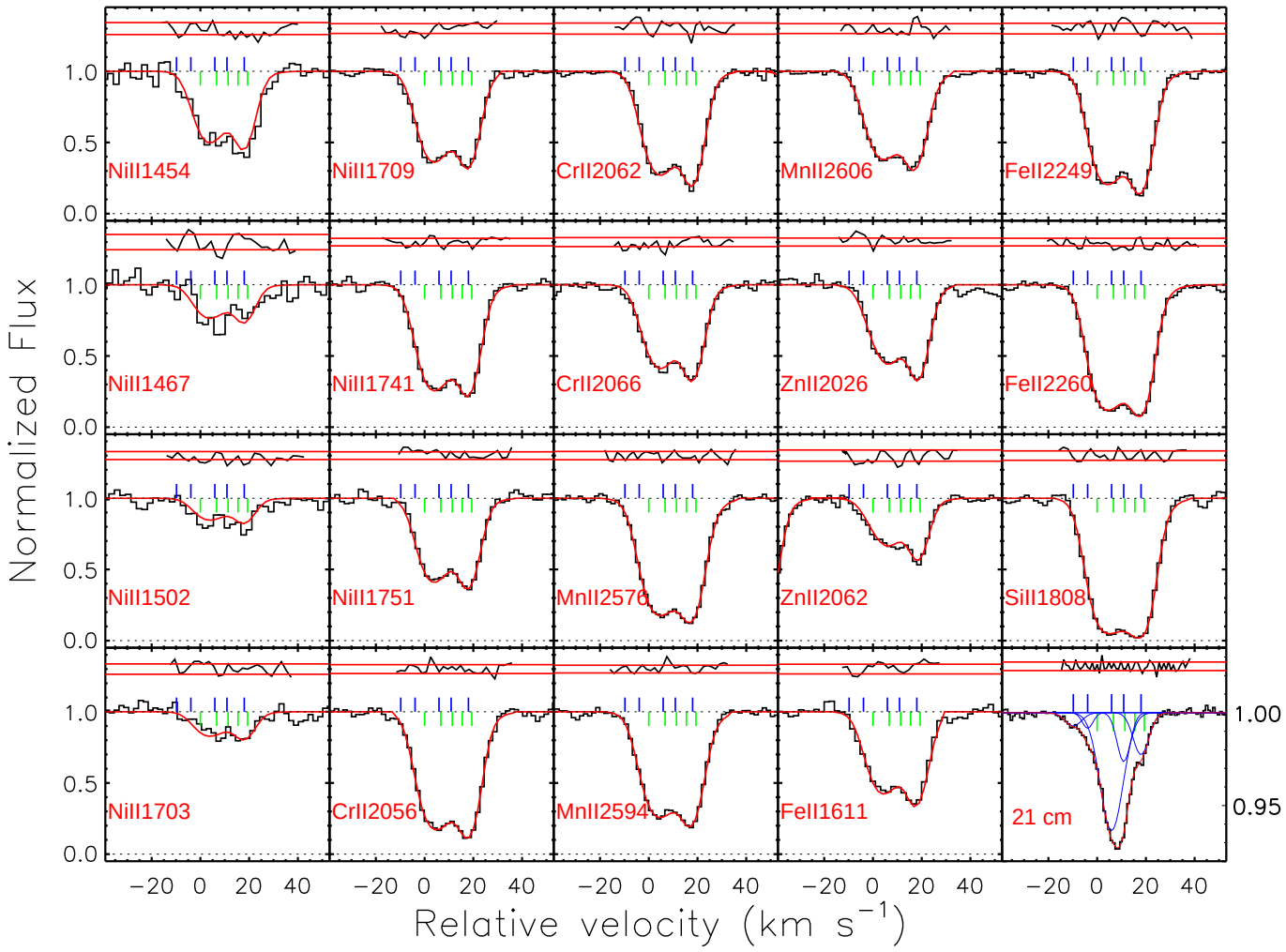

Figure 6. Voigt profile fits to the absorption profiles of the $z_{abs} \sim 1.37$ system towards J0108−0037. The histogram plot in each panel shows the observed absorption profile of a given transition and the continuous curve is the best Voigt profile fit (or Gaussian fit in the case of 21-cm profiles). Last panel shows the 21-cm absorption profile along with the fitted model and its individual components. The normalized residuals (i.e. ([data]−[model]) / [flux error]) for each fit is shown in the top of each panel along with the 1σ horizontal line.

Upper vertical tick marks indicate the position of 21-cm absorber components and lower vertical tick marks indicate different optical-UV velocity component.

of the 21-cm absorption feature even at this higher resolution is consistent with a single component (see Fig. 4). This is the simplest profile in our sample. It is best fitted with a single component at $z_{21} = 1.1730206(17)$. The typical error in the redshift measurement is ∼230 m s^{-1}. As there are 4 individual spectra we also performed a fit using errors that are the rms of the fluxes measured in the different spectra. The fit obtained using these errors gives $z_{21} = 1.1730212(20)$ which is consistent with the above quoted measurement. In Table 4 we also provide results of independent fits to RR and LL spectra. The z_{21} measurement based on the RR spectrum is higher than the one obtained from the LL spectrum with a relative off-set of 1.3±0.6 km s^{-1}. We find this is mainly due to one of the RR spectra being affected by low level RFI. While this spectrum does not influence the weighted mean I-spectra, the combined RR spectrum is appreciably affected by this. Combining all the spectra but this affected spectrum yields $z_{21} = 1.1730188(25)$ (i.e with a redshift error corresponding to 344 m s^{-1}). This is the z_{21} we use to derive $\Delta x/x$ for this system.

4 VOIGT PROFILE FITTING OF UV LINES

In this section we describe the Voigt profile fitting of the UV absorption lines and discuss the individual systems in detail.

4.1 System at $z_{abs} \sim 1.37$ towards J0108−0037

J0108−0037 is one of the brightest quasar in our sample with SDSS r-band magnitude of 17.5. The SNR in the continuum close to the absorption lines used for measuring redshifts is usually larger than

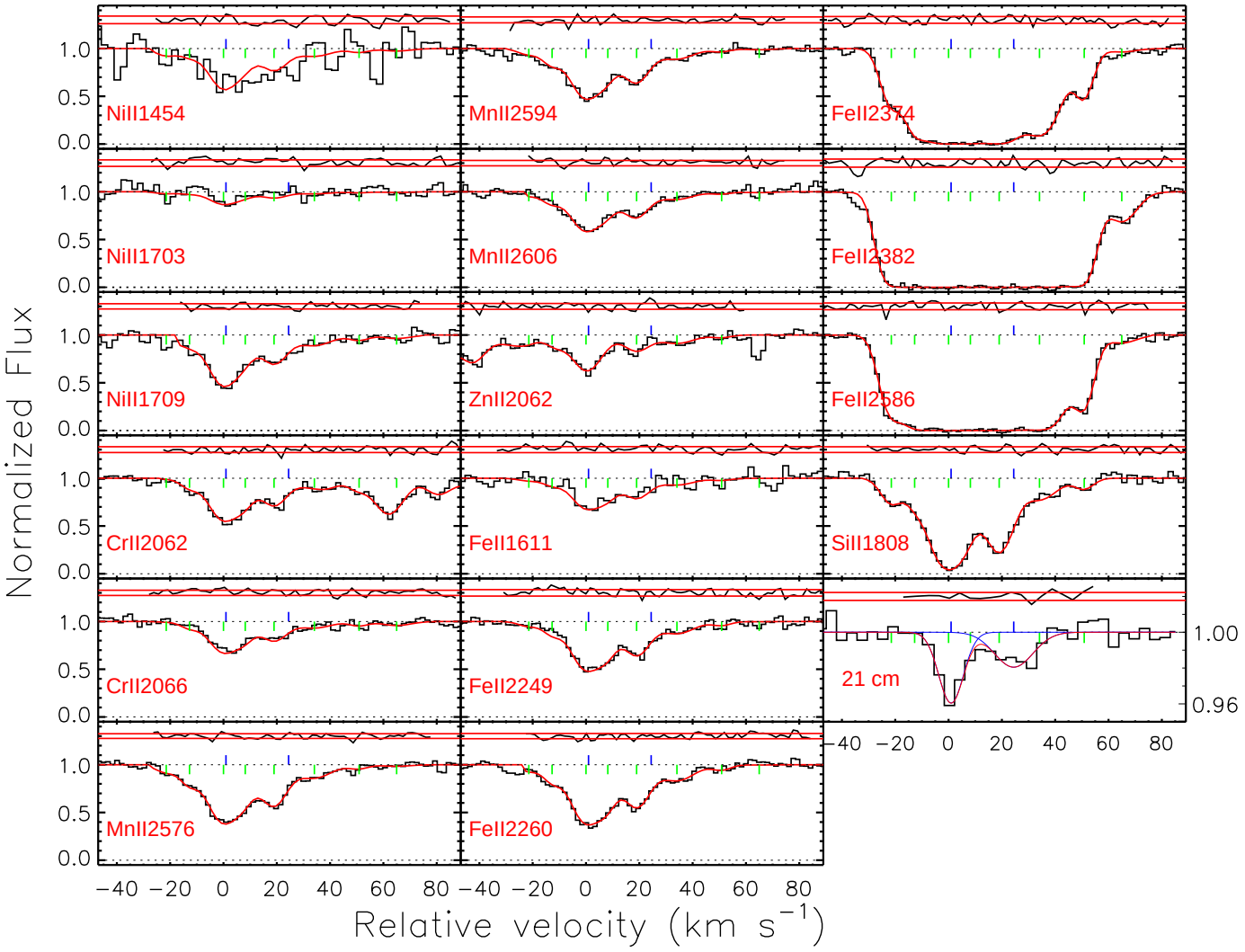

Figure 7. Same as Fig. 6 for $z_{abs} \sim 1.33$ Mg II system towards J1623+0718.

30 for this system. The absorption profiles of all singly ionized transitions used in the Voigt profile fits are shown in Fig. 6. Interestingly many transitions of Ni II are detected in this system. This could allow one to measure $\Delta\alpha/\alpha$ by using only Ni II transitions once accurate values of rest frame wavelengths, oscillator strengths, and sensitivity coefficients are available. Apart from Ni IIλ1467,1502,1703, other absorption profiles are very strong. Absorption profiles of Fe IIλ1608,2344,2374,2382,2586,2600 in our final combined UVES spectra are highly saturated and have not been used for redshift measurement. We have fitted this system with two, three, four, and five components to find the optimal fit. The reduced χ^2 are respectively, 1.60, 1.42, 1.28, and 1.23. Increasing the number of components does not lead to any better fit. Therefore we consider the fit with five components as the best fit for this absorbing system. From our best fit, there are two strong UV absorption components (at v = 6.4 and 19.5 km s^{-1} in Fig. 6) with approximately the same column density of metals. This means, unlike in other cases discussed here, a unique identification of the stongest UV component to be associated with the strongest 21 cm component is highly questionable. Even though both 21-cm and UV absorption lines span the same velocity range there is no one to one correspondence between the two. This could mean that the 21-cm optical depth does not scale with the column density of metal lines. To illustrate this we plot in the bottom right panel of Fig. 6 a five component fit of the 21 cm absorption profile. This could mean as well that additional contribution to 21-cm absorption comes from gas that is not probed by the optical sight line. As the morphology of the background source is complex, we can not rule out that the differences in the absorption profiles are due to the fact that the optical and radio sight lines probe different volumes of the absorbing gas. Therefore, because of the degeneracy introduced by this peculiar profile and the complex morphology of the radio emission we do not use this system for $\Delta x/x$ measurements.

4.2 System at $z \sim 1.33$ towards J1623+0718

J1623+0718 with SDSS r-band magnitude of ~17.5 is another bright quasar in our sample. The velocity plots of some of the

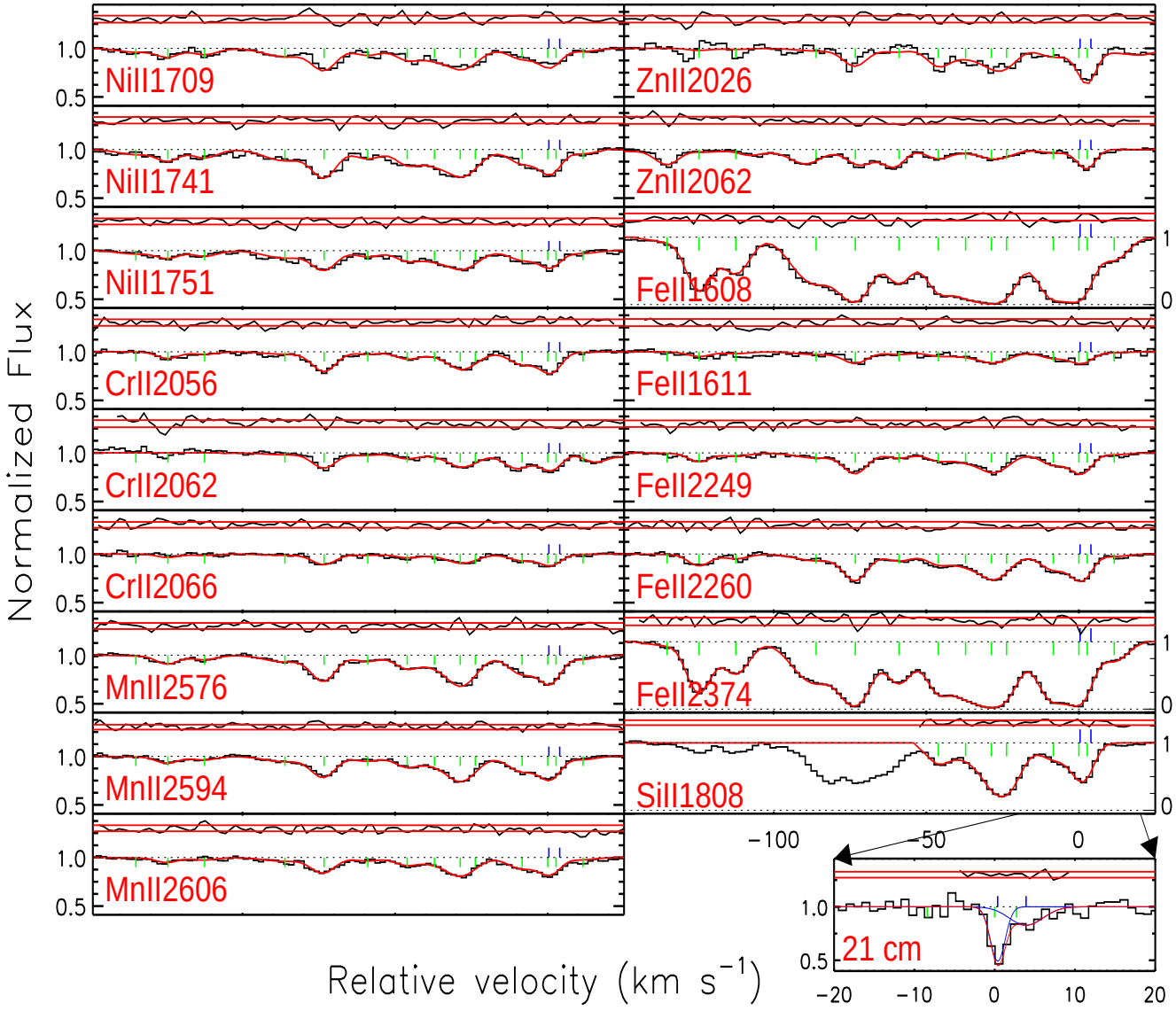

Figure 8. Same as Fig. 6 for the z_{abs}∼1.36 Mg II absorber towards J2340−0053 and for the VLT/UVES. In the bottom right corner panel we zoom over 40 km s^{-1} to show the 21-cm absorber with the two components fit overplotted.

species detected from the z_{abs}∼1.33 system are shown in Fig. 7. The SNR in the continuum close to absorption profile of Ni IIλ1454 is ∼10, and it is higher than 30 close to Fe IIλ2586. The absorption profiles of weak metal transitions like Si IIλ1808 are spread over 80 km s^{-1}. The 21-cm absorption including the broad component is spread over the same velocity range. From visual inspection it is clear that the strongest metal absorption component coincides well with the main narrow 21-cm component.

The optical absorption profiles suggest the presence of additional weak components in the wings (at v∼53 and ∼−20 km s^{-1}). We constrain the component structure in the wings from the strong Fe II lines for which the wings are apparent. The best fitted Voigt profile shown in Fig. 7 has a reduced χ^2 of 1.04. The measured redshift of the strongest metal component in the 21-cm velocity range is z_{abs} = 1.3356684(19) with the typical redshift error of 240 m s^{-1} (see Table 5).

As can be seen, the main component in the metal absorption is broad and may contain additional hidden narrow components. Therefore, we repeated the fits with additional components injected around the main component. The reduced χ^2 does not change with the addition of these new components. There is however a minor change in the absorption redshifts, albeit with increased errors, for the strongest component we find z = 1.3356675(47) with an error of ∼600 m s^{-1}. This is the UV absorption redshift and associated uncertainty we consider for $\Delta x/x$ measurement.

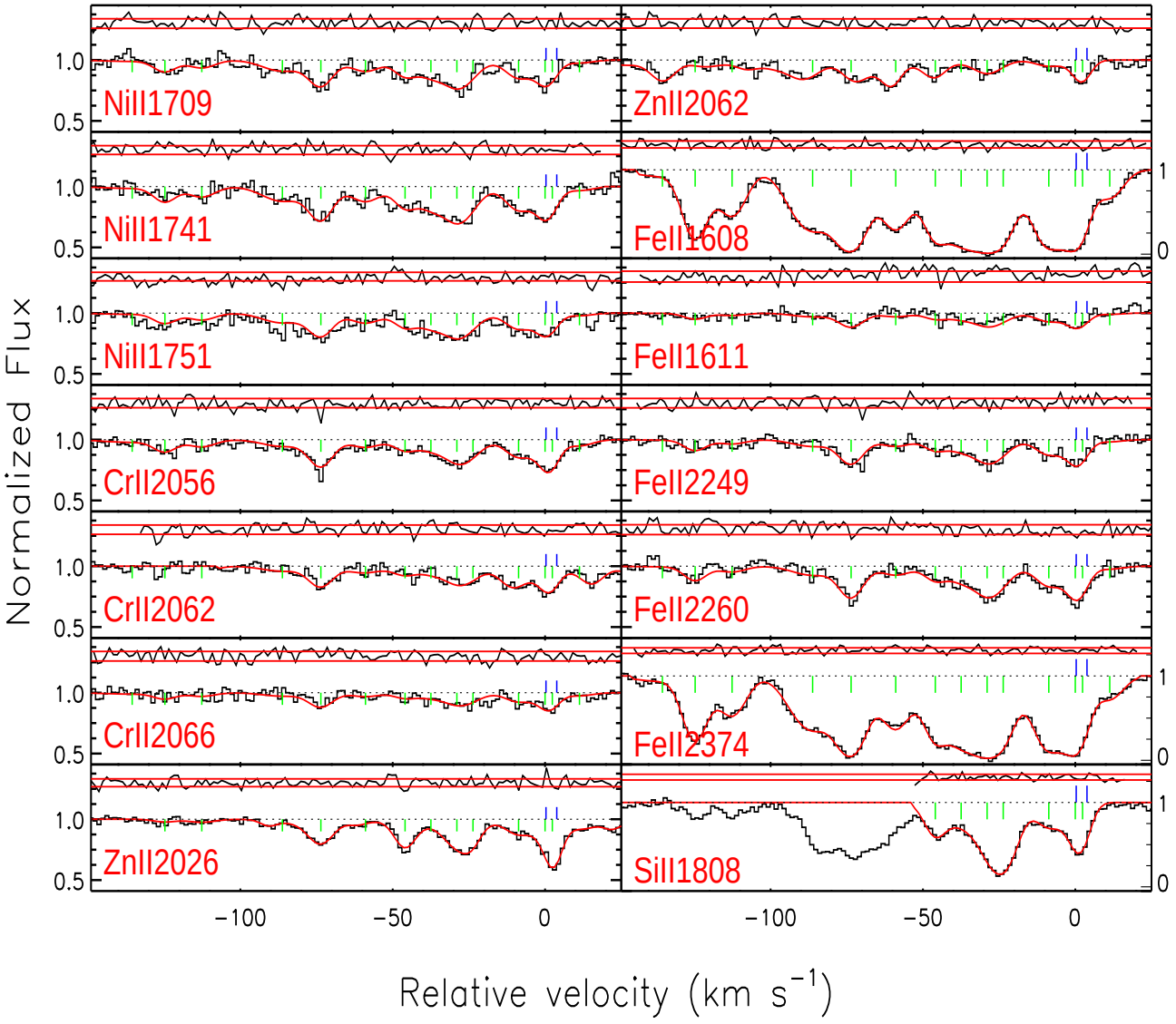

Figure 9. Same as Fig. 6 for the z_{abs}∼1.36 Mg II absorber towards J2340−0053 and for Keck/HIRES.

4.3 System at z_{abs}∼1.36 towards J2340−0053

In addition to our VLT/UVES spectrum we have also analysed the Keck/HIRES spectrum of this object. The velocity plot of different ions detected in this system is shown in Fig. 8 and Fig. 9. The SNR in the UVES continuum is ∼40 close to Ni IIλ1709 and can be larger than 60 close to Mn II absorptions. The absorption lines of singly ionized species are spread over ∼150 km s^{-1}. Unlike in the case of J1623+0718 and J0108−0037 the 21-cm absorption is very much narrower than the UV absorption lines. However, as pointed out by Gupta et al. (2009), the metal component associated with the 21-cm component is well detached. In particular the component is well defined by Si IIλ1808 and Zn II lines. Note, we have not fitted the absorption profile of Si II for $v < -55$ km s^{-1} as this region is contaminated by absorption from another intervening system. The fit has a reduced χ^2 of 1.3. The overall profile is fitted with 14 Voigt profile components and the absorption coinciding with the 21-cm absorption requires two narrow components.

The redshifts of the two UV-optical components in our UVES spectrum that are closer to 21-cm absorption are 1.3608565(16) and 1.3608781(19). The former happens to be the stronger absorption component to be associated to the stronger 21-cm absorption component. The redshift errors due to Voigt profile fitting correspond to 200 and 240 m s^{-1} for these components. The redshifts measured from the HIRES spectrum, 1.3608572(36) and 1.3608759(40), are consistent with those derived from the UVES spectrum. The fitting errors in the redshifts for the HIRES data are 457 and 508 m s^{-1} respectively.

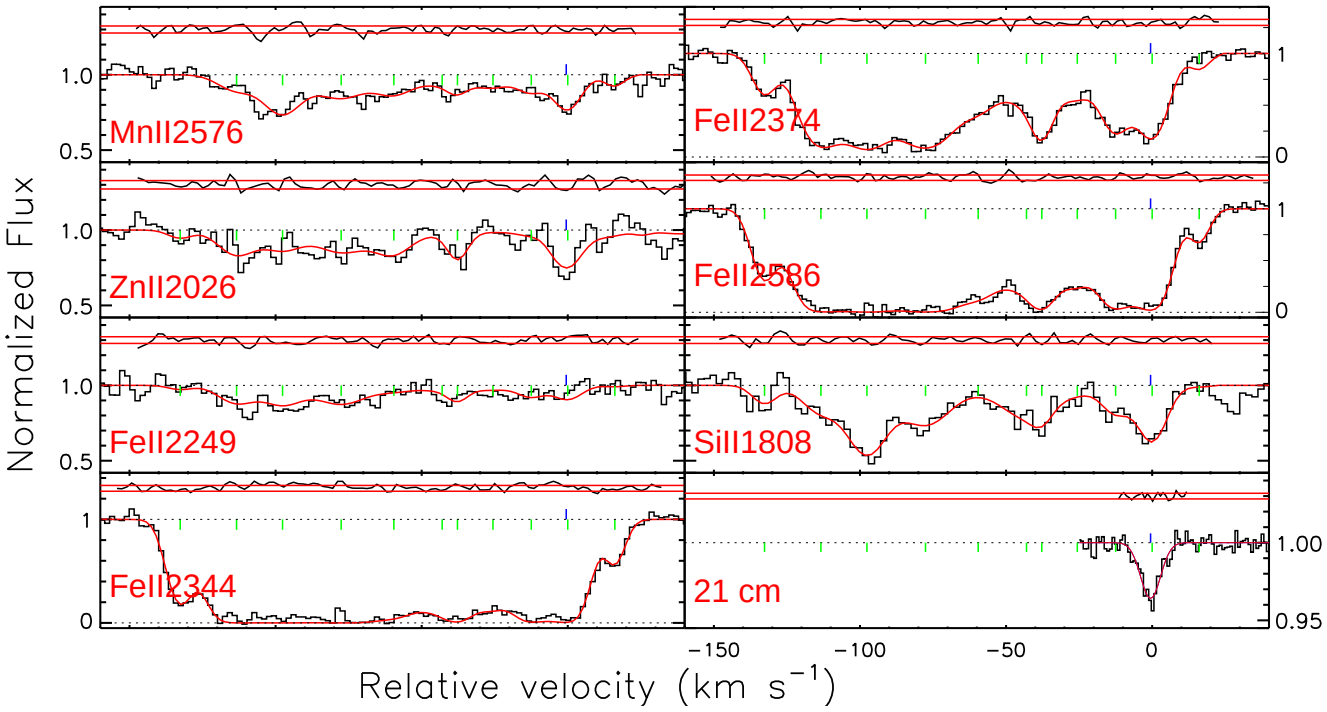

Figure 10. Same as Fig. 6 for the $z_{\rm abs}$~1.17 Mg II absorber towards J2358−1020.

4.4 System at $z_{\rm abs}$ ~ 1.17 towards J2358−1020

J2358−1020 with an r-band SDSS magnitude of 18.7 is one of the faintest quasars in our sample. The SNR in the UVES spectrum is at best $\lesssim$25. As it can be seen in Fig. 10 the absorption profiles are spanning more than 150 km s^{-1}. Absorption profiles of Cr IIλ2056,2062,2066, Zn IIλ2062, Mn IIλ2594,2606 are not used in the fit as they are weak or located in regions of poor SNR. As there are weak components at v~−140 and 15 km s^{-1}, we included two core-saturated profiles, Fe IIλ2344 and Fe IIλ2586, to be able to fit the overall profile. Similar to the case of J2340−0053 the metal component coinciding with the 21-cm absorption seems to be well detached from other components and is well fitted with a single Voigt profile component. This is apparent for Si IIλ1808, Zn IIλ2026, and Mn IIλ2576. The overall fit has 11 Voigt profile components with a reduced χ^2 of 1.2.

The redshift of the stronger absorption component that we associate with the 21-cm absorption is 1.1730227(29). The redshift error from line fitting is ~400 m s^{-1}.

4.5 System at $z_{\rm abs}$ ~ 1.56 towards J0501−0159

J0501−0159 is a faint quasar with an r-band magnitude of 19.33. Similar to the case of J2340−0053 we have spectra obtained with VLT/UVES as well as Keck/HIRES. Fig. 11 presents the velocity plot of different absorption profiles detected in this system. The top and bottom panels show the VLT/UVES and Keck/HIRES spectra respectively, along with their best fit profiles. Although the final combined UVES/VLT spectrum is made of 10 exposures each of more than 3300 s of exposure time, the typical SNR is only $\lesssim$20. Apart from those Fe II lines that are shown in Fig. 11 other Fe II lines are highly saturated or have poor SNR. Associated Ni II absorption lines are very weak and are not used for the Voigt profile fitting. Some of them are located in the Lyman-α forest, others are either contaminated or have poor SNR and therefore have not been included in the fit. Our best fit is shown in Fig. 11 and has a reduced χ^2 of 1.0.

It can be seen in Fig. 11 that the strongest 21-cm component coincides with the strongest metal component seen in the absorption profiles of undepleted species like Zn II and Si II. The redshifts of the UV-optical component in UVES and HIRES data are, respectively, 1.5605354(43) and 1.5605398(276) with errors of 503 m s^{-1} and 3234 m s^{-1}. The two measurements agree within 1.0σ.

5 CONSTRAINING $\Delta x/x$

In this section we present $\Delta x/x$ measurements for individual systems and discuss the associated errors in detail. We measure $\Delta x/x$ using,

$$\frac{\Delta x}{x} = \left(\frac{z_{\rm UV} - z_{21}}{1 + z_{21}}\right), \quad (1)$$

where $z_{\rm UV}$ is the redshift of the UV-optical component as given in column 2 of Table 5 and z_{21} is the redshift of the the 21-cm component as given in column 3 of Table 4. Usually the metal absorption has a larger velocity spread compared to that of 21-cm absorption. So to associate the UV-optical absorption (i.e. $z_{\rm UV}$) to the 21-cm component we use the stronger absorption component in the velocity range of 21-cm absorption. In all cases discussed here the UV-optical absorption clump associated to the 21-cm absorption is easily identifiable. The statistical error due to the fits, $\sigma(\frac{\Delta x}{x})$, is calculated as:

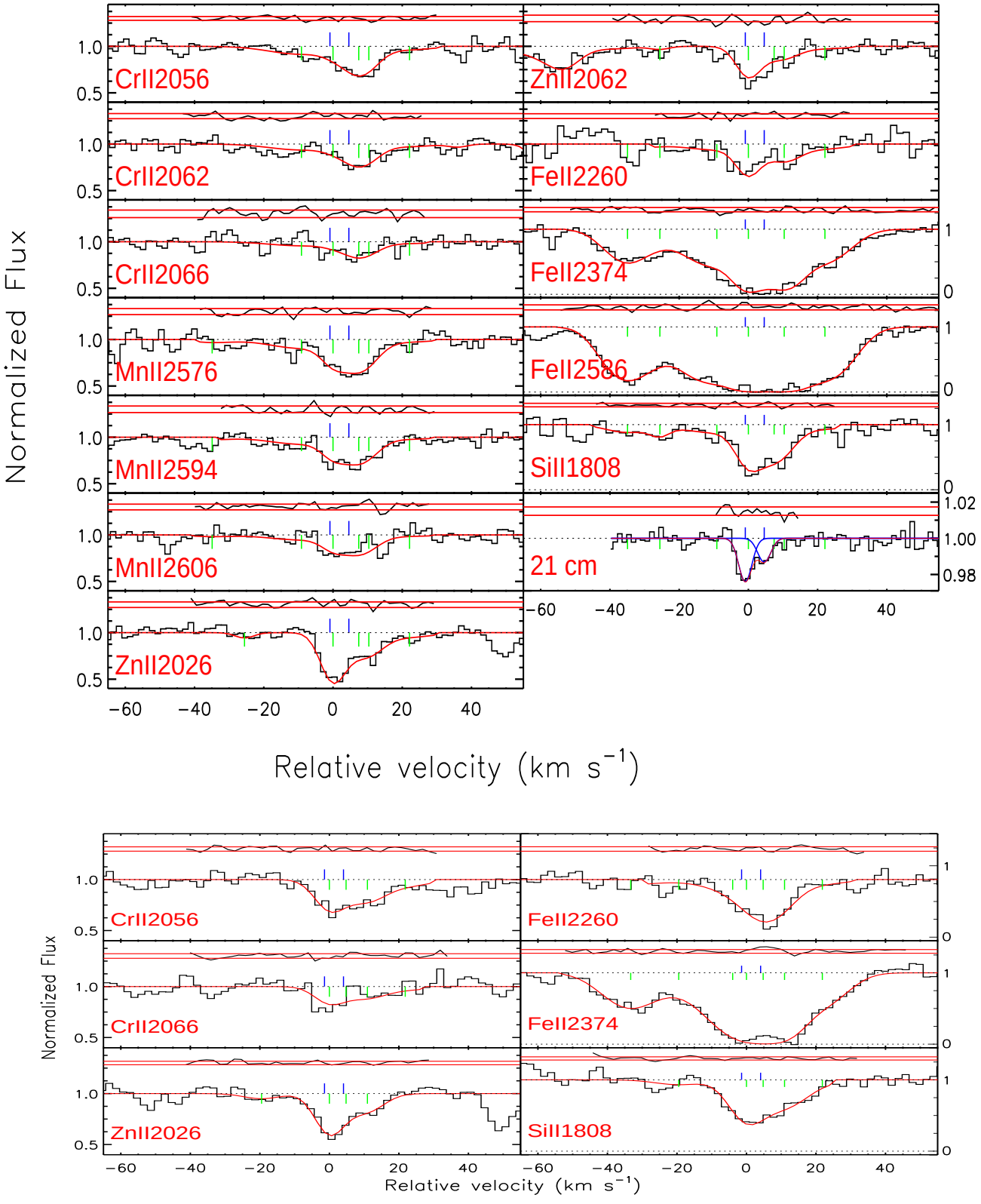

Figure 11. Same as Fig. 6 for the z_{abs}~1.56 Mg II absorber towards J0501−0159 from VLT/UVES spectrum (top) and HIRES/Keck spectrum (bottom).

Table 5. Results of repeated Voigt profile fitting analysis.

Quasar	$z_{\rm UV}$†	δv (km s^{-1})	$\delta v_1^\dagger$ (km s^{-1})	id	$\delta v_2^\dagger$ (km s^{-1})	id	$\delta v_3^\dagger$ (km s^{-1})	id	$\delta v_4^\dagger$ (km s^{-1})	$\delta v_5^\dagger$ (km s^{-1})
(1)	(2)	(3)	(4)	(5)	(6)	(7)	(8)	(9)	(10)	(11)
J1623+0718	1.3356684(19)	0.24	−0.02±0.23	d2,e1,e5	+0.34±0.31	d5	+0.36±0.26	d2,d3,d7,d8,e5,c2	—-	+0.23±0.22
J2340-0053	1.3608565(16)	0.20	+0.26±0.18	d2,f1	−0.22±0.19	d8	−0.48±0.33	e7,a,d3,c1	+0.09±0.46	−0.07±0.15
J2358-1020	1.1730227(29)	0.40	+0.26±0.47	f1,d4	−0.01±0.37	d9	−0.54±0.44	d5,d6	—-	−0.02±0.23
J0501−0159	1.5605354(43)	0.50	+0.35±0.27	b2,b3,d4,c3	+0.26±0.30	d9	+0.15±0.67	b3,a,d3,d8,c2	−0.52±3.23	+0.07±0.17

Column 1: Source name. Column 2: The absorption redshifts and associated error (in brackets) measured using our VLT/UVES spectrum. Column 3: error in the redshift measurement given in Column 2 in km s^{-1}. Column 4: measured velocity offset when excluding weak transitions (as defined in Table. 2) listed in Column 5. Column 6: measured velocity offset when a saturated line (with ids given in column 7) is included in the fit. Column 8: Velocity offset measured after excluding the absorption lines (whose ids are given in column 9) far away from the ThAr lamp lines used for wavelength calibration. Column 10: Measured velocity offset for the redshift measured using Keck/HIRES spectrum. Column 11: Mean and standard deviation of measured redshifts after removing one exposure from combined spectra (see Fig. 12).
† all the velocities and associated errors are calculated with respect to the main redshift given in the second column.

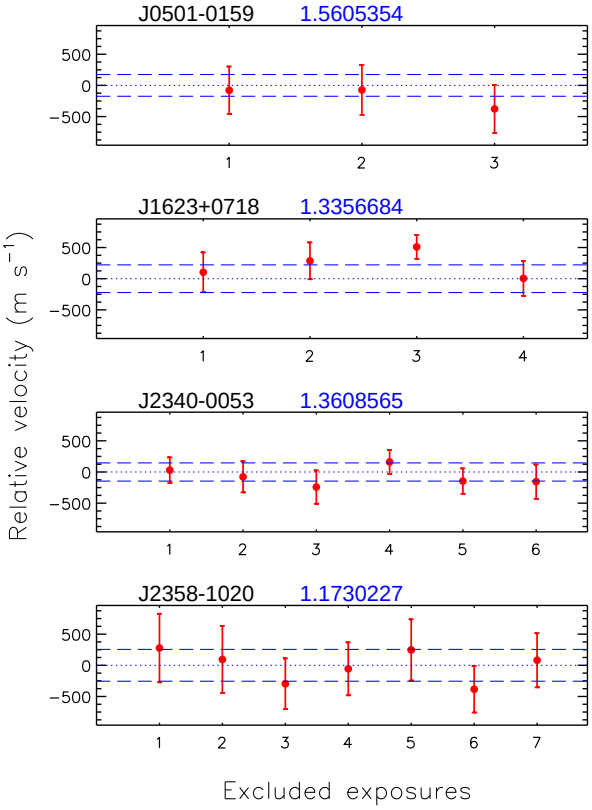

Figure 12. Results of an experiment consisting of measuring the shifts in the observed redshift as a consequence of retrieving one exposure when combining the different exposures to obtain the final quasar spectrum. We only show those components that are used for measuring $\Delta x/x$. Abscissa in each panel indicates the missing exposure(s). The zero of the y-axis is taken at the redshift (indicated at the top of each panel) measured in the spectrum obtained by combining all exposures (dotted line). Short-dashed lines shows the 1σ error on this redshift.

$$\sigma(\frac{\Delta x}{x}) = \frac{1}{1+z_{21}}\sqrt{\left(\left(\frac{1+z_{UV}}{1+z_{21}}\right)^2 \times \sigma^2_{z_{21}} + \sigma^2_{z_{UV}}\right)}, \quad (2)$$

in which $\sigma_{z_{\rm UV}}$ and $\sigma_{z_{21}}$ are the errors on $z_{\rm UV}$ and z_{21} respectively. In the case of $\sigma_{z_{21}}$ we consider the contributions of statistical (Table. 4) and systematic uncertainties (Table 3), the latter being smaller ($\sim$ 122 m s^{-1}) than the former ($\geq$ 300 m s^{-1}). To estimate the systematic errors in the optical redshifts we carry out a number of tests whose results are summarized in Table 5 and also in the tables of the Appendix (see Section 2.1 for more detail). In columns (4), (6), and (8) of Table 5 we give velocity offsets measured with respect to $z_{\rm abs}$ given in column (2) using repeated Voigt profile fitting after, respectively, excluding weak lines, including saturated lines, and excluding the absorption lines with no ThAr line within 50 km s^{-1} of that optical component assigned to 21-cm component. The reference to the corresponding lines are given in the preceding column. The results of these tests are sensitive to the intra-order wavelength calibration errors. To be on the conservative side we consider the maximum error found here as a measure of the systematic error introduced from intra-order shifts ($\sigma_{\rm e}$).

In column (11) of Table 5 we give the mean velocity offset found by repeated Voigt profile fitting of lines after excluding one of the exposures (See also Fig. 12). Tables in the Appendix also summarize the results of cross-correlation analysis between the individual exposures and the combined spectra. The results of the last two exercises (exposure removal and cross-correlation) are sensitive to any constant shift between different exposures. Therefore we consider the maximum of these two shifts as an estimate of the constant shift error in the wavelength calibration ($\sigma_{\rm c}$). The final systematic error for each sight line is taken as the quadratic sum of the two systematic errors. The approach taken here is conservative to allow for maximum uncertainty in the measurement of $z_{\rm UV}$. We summarize the values of $\sigma_{\rm e}$ and $\sigma_{\rm c}$ for individual systems in Table 6 where these errors are converted from velocity shifts to $\Delta x/x$. In column (7) of Table 6 we present the total systematic error, $\sigma_{\rm sys}$, which is calculated from the quadratic sum of $\sigma_{\rm e}$, $\sigma_{\rm c}$ and 122 m s^{-1} we found from 21-cm analysis.

6 RESULTS AND CONCLUSIONS

In Table 6 we summarize the $\Delta x/x$ measurements in individual systems. We recollect that the values are obtained under the assump-

Table 6. $\Delta x/x$ measured (in units of 10^{-6}) from different absorption systems

Quasar	z_{abs}	UVES							Keck	dipole		$\Delta(\Delta\alpha/\alpha)$
		$\Delta x/x$	σ_{stat}	σ_c	σ_e	σ_{sys}	σ_{tot}	$\Delta\alpha/\alpha$	$\Delta x/x$	Θ	$\Delta\alpha/\alpha$	
(1)	(2)	(3)	(4)	(5)	(6)	(7)	(8)	(9)	(10)	(11)	(12)	(13)
J1623+0718	1.3356	−3.7	3.0	1.0	1.2	1.6	3.4	−1.8±1.7	....	66.0	+3.9±1.6	+5.7±2.3
J2340−0053	1.3608	−1.3	0.9	0.7	1.6	1.7	2.0	−0.6±1.0	−1.0±1.6	90.6	−0.1±1.2	+0.5±1.6
J2358−1020	1.1730	+1.8	1.8	0.8	1.8	2.0	2.7	+0.9±1.4	....	84.9	+0.8±1.1	−0.1±1.8
J0501−0159	1.5605	+3.0	2.1	0.6	2.2	2.3	3.1	+1.5±1.6	+4.7±10.9	119.0	−5.2±1.8	−6.7±2.4
		UVES							Keck			
simple average		0.0 ±1.5							+1.8 ±2.8			
weighted average		−0.1 ±1.3							−0.9 ±1.6			

Column 1: Object name. Column 2: absorption redshift. Columns 3-8: $\Delta x/x$ measurement, associated statistical and systematic errors (as discussed in Section 5) respectively. Column 9: $\Delta\alpha/\alpha$ calculated based on the final values for $\Delta x/x$ assuming constancy of other constants. Column 10: $\Delta x/x$ measurements based on Keck/HIRES data. Column 11 and 12: angular distance in degrees between the quasar sight line and the best fitted dipole position from Webb et al. (2011) and the predicted value for $\Delta\alpha/\alpha$ based on dipole. Column 13: difference between our measurement and the prediction from dipole and its associated error.

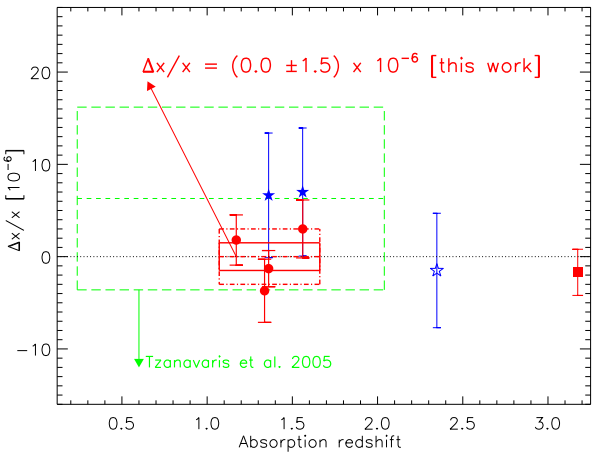

Figure 13. Comparison of our $\Delta x/x$ measurements with three other measurements in the literature. Filled circles are our measurements and the filled square is from Srianand et al. (2010) using a 21-cm absorber at $z \sim 3.174$ along the line of sight of J1337+3152. The dashed-dotted box corresponds to the standard deviation of our four measurements The 1σ error around the mean is shown as a solid box. The dashed line and long-dashed box are the $\Delta x/x$ and its error measured by Tzanavaris et al. (2007). The filled and empty stars are respectively from Kanekar et al. (2010) and Kanekar et al. (2006).

tion that the strongest UV and 21-cm absorption are produced by the same gas. The final errors in $\Delta x/x$ for our VLT/UVES measurements given in column (8) are the quadratic sum of the statistical and systematic errors. We find the simple mean of $\Delta x/x$ regardless of the associated errors in individual measurements to be $(0.0\pm1.5)\times10^{-6}$ with an rms of 3.0×10^{-6} around the mean. A constant $\Delta x/x$ of 0.0×10^{-6} has a reduced χ^2 of 1.0 for our four UVES measurements that shows the estimated errors in $\Delta x/x$ are not underestimated. If we apply the standard procedure of weighting the data points by their inverse square errors (given in column (8) of Table 6), we get $-(0.1 \pm 1.3) \times 10^{-6}$.

Our VLBA images suggest that two of the quasars in the sample (i.e J1623+0718 and J0501−0159) may have resolved structures at milliarcsec scale containing more than 50% of the flux. This may imply that if the absorbing gas is extended then some additional 21-cm absorption can originate from the gas that is not probed by the optical sight lines. However in the remaining two quasars this is not the case as most of the flux is recovered in the unresolved VLBA component. If we only use these two cases we derive $\Delta x/x = +(0.2\pm1.6)\times10^{-6}$. This is very much consistent with what we find using all the four systems. Therefore the analysis presented here does not find any statistically significant variation in x and this null result may not be related to systematics due to radio structure.

There are two quasars for which we have spectra from both VLT and Keck. As can be seen from Table 6 in both cases the VLT and Keck measurements are consistent with each other with Keck measurements having larger statistical uncertainties. The mean $\Delta x/x$ from VLT/UVES data of $(0.0\pm1.5)\times10^{-6}$ is consistent with $\Delta x/x = +(1.8\pm2.8)\times10^{-6}$ from Keck/HIRES data where we could not include the systematic error. This is also the case for the weighted means.

In Fig. 13 we compare our $\Delta x/x$ results with other $\Delta x/x$ measurements from the literature. Filled circles are our measurements. The dashed-dotted rectangular box indicates the mean and standard deviation of our measurements. The solid rectangular box gives the mean and final error on it when combining the 4 measurements. The green box with the dashed line gives the weighted mean and 1σ found by Tzanavaris et al. (2007). The two filled stars are from Kanekar et al. (2010) and the empty star is from Kanekar et al. (2006). The data point at $z \sim 3.174$ is from Srianand et al. (2010).

The better accuracy reached in our study is mainly due to the following reasons: (1) Systems are chosen to have narrow 21-cm absorption components. (2) Three of the quasars have high resolution (R∼45000) and high SNR UV-optical spectra obtained specifically for constraining $\Delta x/x$ with attached ThAr calibration lamps for each spectrum. This minimizes the systematic error of wavelength calibration. (3) Very high (∼1 km s^{-1}per channel) or high ($2-4$ km s^{-1}per channel) resolution 21-cm spectra are used. (4) As we could get repeated observations for 21-cm absorptions we are able to identify the RFI related problems in the absorption profiles. (5) We also estimate $\Delta x/x$ by using only absorbers for which the background sources are unresolved even at milliarcsec scale in VLBA images.

Although tight constraints on the variation of fundamental

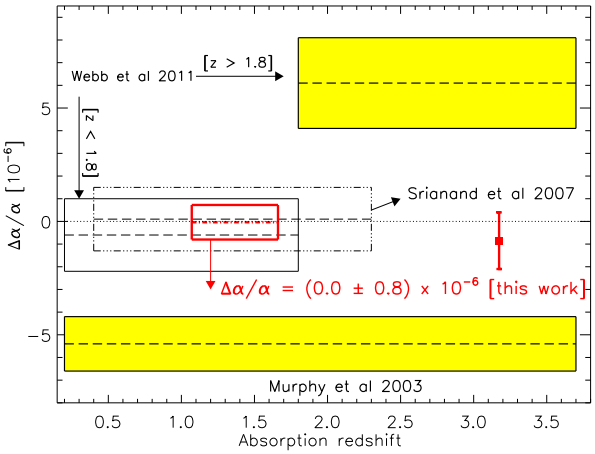

Figure 14. Comparison of $\Delta\alpha/\alpha$ estimated in this work with other measurements in literature. The dashed dotted line and the surrounded solid box show our measured $\Delta\alpha/\alpha$ and its error and the filled square is the one from Srianand et al. (2010) based on the same method and assuming μ and g_p are not changing with time.

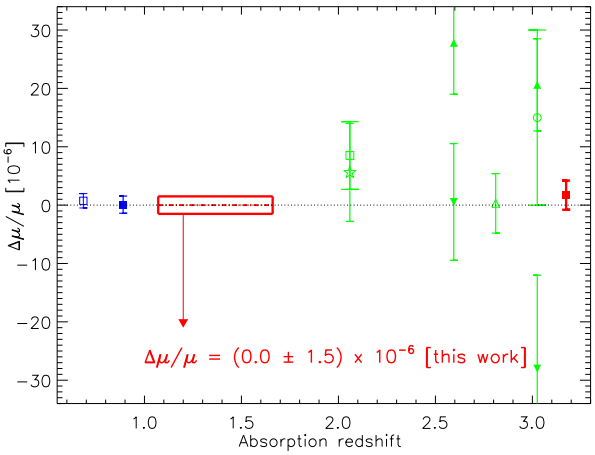

Figure 15. Comparison of $\Delta\mu/\mu$ estimated in this work with other measurements in literature. The dashed dotted line and the surrounded solid box show our measured $\Delta\mu/\mu$ and its error based on our $\Delta x/x$ measurements and assuming α and g_p do not vary. Apart from the filled square at $z\sim3.2$ which is calculated from $\Delta x/x$ of Srianand et al. (2010) with the assumption of non-variation of other constants, the rest of the measurements for $z > 2$ are based on the analysis of H_2 electronic transitions. The empty triangle towards up is from King et al. (2011), empty star from Malec et al. (2010), empty square with a large bar from van Weerdenburg et al. (2011), empty circle with a large bar from Wendt & Molaro (2011), filled triangles towards down from Thompson et al. (2009), and filled triangles towards up from Reinhold et al. (2006). The two measurements at $z \leq 1$ are based on the molecular inversion and rotational transitions. The filled and empty squares are from Henkel et al. (2008) and Murphy et al. (2008) respectively.

constants are obtained by comparing 21-cm and UV-optical redshifts, the method is not exempt of systematics as all other methods in this field. As it is has already been discussed, the main source of uncertainty on $\Delta x/x$ is related to the assumption used to associate one of the several UV-optical components to the 21-cm absorption. By choosing absorbers with compact background radio sources at mas scale one can minimize the uncertainties related to the possibility that optical and radio sightlines are different. Different methods have been implemented to associate the UV-optical component to the 21-cm one. Tzanavaris et al. (2007) associated the pixel with strongest UV-optical optical depth to the pixel with strongest 21-cm optical depth. In this work we follow the same idea but using components of simultaneous Voigt profile fitting models. Using the same method as Tzanavaris et al. (2007), we find $\Delta x/x = (3.6 \pm 3.1) \times 10^{-6}$. Keeping this in mind we will now discuss the implication of our constraint on $\Delta x/x$ on the variation of individual constants that constitute x.

As $x = g_p\alpha^2/\mu$, its variation can be related to the variation of g_p, α, and/or μ via $\Delta x/x = \Delta g_p/g_p + 2 \times \Delta\alpha/\alpha - \Delta\mu/\mu$. Therefore the constancy of x can be related either to the constancy of all the three constants, g_p, α and μ, or to some complicated combination of variations of these constants with an overall null effect on x.

Assuming μ and g_p are constants then our measured $\Delta x/x$ translates to $\Delta\alpha/\alpha = (0.0 \pm 0.8) \times 10^{-6}$ which is one of the most stringent constraint on the variation of α. In Fig 14 we summarize the available constraints on $\Delta\alpha/\alpha$ from the literature. It is clear that our measurements are consistent with $\Delta\alpha/\alpha = (0.1 \pm 1.5) \times 10^{-6}$ (and a factor 2 better than that) found by Srianand et al. (2007) and with the results of Webb et al. (2011) for $z \leq 1.8$ UVES data. Even if we use the conservative approach of Tzanavaris et al. (2007) we get $\Delta\alpha/\alpha = (1.8 \pm 1.5) \times 10^{-6}$ which is as good as the results from the MM method.

Webb et al. (2011) used a combined set of absorbers observed with VLT/UVES and Keck/HIRES to conjecture about the possible presence of a spatial dipole pattern in the variation of α. Their best fitted model indicates a spatial dipole in the direction with right ascension 17.5±0.9 h and declination -58 ± 9 deg, significant at the 4.2σ level with $\Delta\alpha/\alpha = Ar\cos(\Theta)$, where $A = (1.1 \pm 0.25) \times 10^{-6}$GLyr^{-1}, $r(z) = ct(z)$, c being the speed of light and $t(z)$ the look back time, and Θ is the angle on the sky between the quasar sight line and the best fit dipole position. We calculated the prediction of this model for our sample using the same cosmology as Webb et al. (2011). We also calculated the error on $\Delta\alpha/\alpha$ using

$$\sigma(\frac{\Delta\alpha}{\alpha}) = \sqrt{\left(\frac{\Delta\alpha/\alpha}{A}\right)^2 \sigma_A^2 + \left(\frac{\Delta\alpha/\alpha}{\cos(\Theta)}\right)^2 \sigma^2_{\cos(\Theta)}}. \quad (3)$$

The measured Θ and accordingly the predicted values for $\Delta\alpha/\alpha$ are presented in columns 11 and 12 of Table 6. Last column of Table 6 shows the difference of $\Delta\alpha/\alpha$ between the dipole and our measurement and its error. For the sight lines towards J1623+0718 and J0501−0159 the dipole predicts a variation of α at, respectively, the $\sim2.4\sigma$ and 2.9σ level. In both cases, our null results on the α-variation are inconsistent with this dipole prediction at more than 90% confidence level. For the other two sight lines towards J2340−0053 and J2358−1020 our measurements are consistent with null variation as also predicted by the dipole. In the case of J1337+3152 Srianand et al. (2010) measured $\Delta x/x = -(1.7 \pm 1.7) \times 10^{-6}$ for the absorber at $z_{abs} = 3.174$ which translates to $\Delta\alpha/\alpha = -(0.9 \pm 0.9) \times 10^{-6}$. The dipole prediction in this case is $\Delta\alpha/\alpha = -(2.70 \pm 1.9) \times 10^{-6}$ with a difference of $-(1.80 \pm 2.1) \times 10^{-6}$ with the measurement. The difference between these five measurements and the dipole predictions results in a χ^2 of 14.5. The probability of $\chi^2 > 14.5$ is $\sim$ 1% which implies that the existence of a dipole is not favored by our measurements. More independent measurements especially towards systems where the dipole predicts large variations will be useful to confirm/refute the existence of the $\alpha-$dipole at higher significant level.

Assuming that α and g_p have been constant we derive $\Delta\mu/\mu$

$= (0.0 \pm 1.5) \times 10^{-6}$. Fig. 15 compares our results with other direct measurements of $\Delta\mu/\mu$ obtained either using rotational transitions of H_2 and HD molecules (for $z \geq 2.0$) or based on the comparison of NH_3 inversion transitions with some rotational transition lines (e.g. CO, CS, HC_3N; for $z \leq 1.0$). While the constraints we get are not as good as the one obtained using NH_3 they are very stringent compared to those based on H_2 at $z \geq 2$. What is more interesting is that our measurements fill the redshift gap between NH_3 and H_2 based measurements (see Fig. 15).

If we use the 1σ constraints on $\Delta\alpha/\alpha$ found for $z \leq 1.8$ absorbers (from Srianand et al. 2007; Webb et al. 2011) and $\Delta\mu/\mu$ estimated at $z \sim 0.7$ using NH_3 (Kanekar 2011), considering they are valid at $z \sim 1.3$, we get $\Delta g_p/g_p \leq 3.5 \times 10^{-6}(1\sigma)$ from our $\Delta x/x$ measurements.

In summary, using 21-cm and metal UV absorption lines we are able to derive stringent constraints on the variation of α, μ, and g_p. As discussed before the best estimate on $\Delta\mu/\mu$ at z ≤1 is obtained by comparing the frequencies of NH_3 inversion transitions with rotational transitions of other molecules. The existing two measurements are towards the line of sight of two well known gravitationally lensed BL Lacs (B 0218+357 and PKS 1830−211) that show complex radio morphologies. As different transitions occur at different frequencies the dependence of the background radio structure on frequency is an important source of systematic error (see Murphy et al. 2008; Kanekar 2011). Therefore detecting NH_3 and other molecules towards unlensed compact radio sources is important to constrain $\Delta\mu/\mu$. Unlike NH_3 and other complex heavy molecules, 21-cm absorption is more frequently detected towards normal radio sources covering a wide redshift range. The main source of systematics in this method is related to how accurately the 21-cm absorption component is associated to the corresponding metal line component. More measurements towards compact radio sources are needed to address this issue adequately. Future blind searches for 21-cm absorption using the upcoming Square Kilometer Array (SKA) path finders hopefully will provide a large number of suitable targets to perform such measurements.

ACKNOWLEDGEMENT

We would like to thank the anonymous referee for the helpful and constructive comments. We thank GMRT, GBT, and VLBA staff for their support during the observation. GMRT is an international facility run by the National Centre for Radio Astrophysics of the Tata Institute of Fundamental Research. GBT and VLBA are run by National Radio Astronomy Observatory. The VLBA data from 2010 were correlated using NRAO's implementation of the DiFX software correlator that was developed as part of the Australian Major National Research facilities Programme and operated under license. The National Radio Astronomy Observatory is a facility of the National Science Foundation operated under cooperative agreement by Associative Universities, Inc. R. S. and P. P. J. gratefully acknowledge support from the Indo-French Centre for the Promotion of Advanced Research (Centre Franco-Indian pour la Promotion de la Recherche Avancée) under contract No. 4304-2.

REFERENCES

Agafonova, I. I., Molaro, P., Levshakov, S. A., & Hou, J. L., 2011, A&A, 529, A28+

Aldenius, M., 2009, Physica Scripta Volume T, 134, 014008

Bahcall, J. N. & Schmidt, M., 1967, Physical Review Letters, 19, 1294

Briggs, F. H., Wolfe, A. M., Liszt, H. S., Davis, M. M., & Turner, K. L., 1989, ApJ, 341, 650

Carswell, R. F., Jorgenson, R. A., Wolfe, A. M., & Murphy, M. T., 2011, MNRAS, 411, 2319

Chand, H., Petitjean, P., Srianand, R., & Aracil, B., 2005, A&A, 430, 47

Chand, H., Srianand, R., Petitjean, P., & Aracil, B., 2004, A&A, 417, 853

Chand, H., Srianand, R., Petitjean, P., Aracil, B., Quast, R., & Reimers, D., 2006, A&A, 451, 45

Cowie, L. L. & Songaila, A., 1995, ApJ, 453, 596

Dekker, H., D'Odorico, S., Kaufer, A., Delabre, B., & Kotzlowski, H., 2000, in Proc. SPIE Vol. 4008, p. 534-545, Optical and IR Telescope Instrumentation and Detectors, Masanori Iye; Alan F. Moorwood; Eds., pp. 534–545

Dent, T. & Fairbairn, M., 2003, Nuclear Physics B, 653, 256

Dent, T., Stern, S., & Wetterich, C., 2008, Phys. Rev. D, 78, 103518

Dine, M., Nir, Y., Raz, G., & Volansky, T., 2003, Phys. Rev. D, 67, 015009

D'Odorico, S., Cristiani, S., Dekker, H., Hill, V., Kaufer, A., Kim, T., & Primas, F., 2000, in Society of Photo-Optical Instrumentation Engineers (SPIE) Conference Series, Vol. 4005, Society of Photo-Optical Instrumentation Engineers (SPIE) Conference Series, J. Bergeron, ed., pp. 121–130

Dzuba, V. A., Flambaum, V. V., & Webb, J. K., 1999a, Phys. Rev. A, 59, 230

—, 1999b, Physical Review Letters, 82, 888

Edlén, B., 1966, Metrologia, 2, 71

Fey, A. L. & Charlot, P., 2000, ApJS, 128, 17

Fomalont, E. B., Frey, S., Paragi, Z., Gurvits, L. I., Scott, W. K., Taylor, A. R., Edwards, P. G., & Hirabayashi, H., 2000, ApJS, 131, 95

Gupta, N., Srianand, R., Petitjean, P., Bergeron, J., Noterdaeme, P., & Muzahid, S., 2012, ArXiv:1205.4029

Gupta, N., Srianand, R., Petitjean, P., Khare, P., Saikia, D. J., & York, D. G., 2007, ApJ, 654, L111

Gupta, N., Srianand, R., Petitjean, P., Noterdaeme, P., & Saikia, D. J., 2009, MNRAS, 398, 201

Henkel, C., Braatz, J. A., Menten, K. M., & Ott, J., 2008, A&A, 485, 451

Henkel, C., Jethava, N., Kraus, A., Menten, K. M., Carilli, C. L., Grasshoff, M., Lubowich, D., & Reid, M. J., 2005, A&A, 440, 893

Ivanchik, A., Petitjean, P., Varshalovich, D., Aracil, B., Srianand, R., Chand, H., Ledoux, C., & Boissé, P., 2005, A&A, 440, 45

Kanekar, N., 2011, ApJ, 728, L12

Kanekar, N., Prochaska, J. X., Ellison, S. L., & Chengalur, J. N., 2009, MNRAS, 396, 385

—, 2010, ApJ, 712, L148

Kanekar, N., Subrahmanyan, R., Ellison, S. L., Lane, W. M., & Chengalur, J. N., 2006, MNRAS, 370, L46

King, J. A., Mortlock, D. J., Webb, J. K., & Murphy, M. T., 2009, Mem. Soc. Astron. Italiana, 80, 864

King, J. A., Murphy, M. T., Ubachs, W., & Webb, J. K., 2011, MNRAS, 417, 3010

King, J. A., Webb, J. K., Murphy, M. T., & Carswell, R. F., 2008, Physical Review Letters, 101, 251304

Kovalev, Y. Y., Petrov, L., Fomalont, E. B., & Gordon, D., 2007, AJ, 133, 1236

Ledoux, C., Petitjean, P., & Srianand, R., 2003, MNRAS, 346, 209
Levshakov, S. A., 1994, MNRAS, 269, 339
Levshakov, S. A., Centurión, M., Molaro, P., D'Odorico, S., Reimers, D., Quast, R., & Pollmann, M., 2006, A&A, 449, 879
Levshakov, S. A., Molaro, P., Lopez, S., D'Odorico, S., Centurión, M., Bonifacio, P., Agafonova, I. I., & Reimers, D., 2007, A&A, 466, 1077
Malec, A. L., Buning, R., Murphy, M. T., et al., 2010, MNRAS, 403, 1541
Molaro, P., Levshakov, S. A., Monai, S., Centurión, M., Bonifacio, P., D'Odorico, S., & Monaco, L., 2008, A&A, 481, 559
Morton, D. C., 2003, ApJS, 149, 205
Murphy, M. T., Flambaum, V. V., Muller, S., & Henkel, C., 2008, Science, 320, 1611
Murphy, M. T., Webb, J. K., & Flambaum, V. V., 2003, MNRAS, 345, 609
—, 2007, Physical Review Letters, 99, 239001
Murphy, M. T., Webb, J. K., Flambaum, V. V., Prochaska, J. X., & Wolfe, A. M., 2001, MNRAS, 327, 1237
Nave, G. & Sansonetti, C. J., 2011, Journal of the Optical Society of America B Optical Physics, 28, 737
Noterdaeme, P., Ledoux, C., Petitjean, P., & Srianand, R., 2008, A&A, 481, 327
Olive, K. & Skillman, E., 2004, Astrophys. J., 617, 29
Olive, K. A., Peloso, M., & Uzan, J.-P., 2011, Phys. Rev. D, 83, 043509
Olive, K. A., Pospelov, M., Qian, Y.-Z., Coc, A., Cassé, M., & Vangioni-Flam, E., 2002, Phys. Rev. D, 66, 045022
Petitjean, P., Srianand, R., & Ledoux, C., 2000, A&A, 364, L26
Petrov, Y., Nazarov, A., Onegin, M., Petrov, V., & Sakhnovsky, E., 2006, Phys. Rev. C, 74
Prochaska, J. X., Wolfe, A. M., Howk, J. C., Gawiser, E., Burles, S. M., & Cooke, J., 2007, ApJS, 171, 29
Prochaska, J. X., Wolfe, A. M., Tytler, D., et al., 2001, ApJS, 137, 21
Quast, R., Reimers, D., & Levshakov, S. A., 2004, A&A, 415, L7
Reinhold, E., Buning, R., Hollenstein, U., Ivanchik, A., Petitjean, P., & Ubachs, W., 2006, Phys. Rev. Lett., 96, 151101
Rosenband, T., Hume, D., Schmidt, P., et al., 2008, Science, 319, 1808
Savedoff, M. P., 1956, Nature, 178, 688
Srianand, R., Chand, H., Petitjean, P., & Aracil, B., 2004, Physical Review Letters, 92, 121302
—, 2007, Physical Review Letters, 99, 239002
Srianand, R., Gupta, N., Petitjean, P., Noterdaeme, P., & Ledoux, C., 2010, MNRAS, 405, 1888
Srianand, R., Gupta, N., Petitjean, P., Noterdaeme, P., Ledoux, C., Salter, C. J., & Saikia, D. J., 2012, MNRAS, 421, 651
Thompson, R. I., Bechtold, J., Black, J. H., et al., 2009, ApJ, 703, 1648
Tzanavaris, P., Murphy, M. T., Webb, J. K., Flambaum, V. V., & Curran, S. J., 2007, MNRAS, 374, 634
Uzan, J.-P., 2003, Reviews of Modern Physics, 75, 403
van Weerdenburg, F., Murphy, M. T., Malec, A. L., Kaper, L., & Ubachs, W., 2011, Physical Review Letters, 106, 180802
Varshalovich, D. A. & Levshakov, S. A., 1993, Soviet Journal of Experimental and Theoretical Physics Letters, 58, 237
Varshalovich, D. A., Panchuk, V. E., & Ivanchik, A. V., 1996, Astronomy Letters, 22, 6
Varshalovich, D. A., Potekhin, A. Y., & Ivanchik, A. V., 2000, ArXiv Physics e-prints
Webb, J. K., Flambaum, V. V., Churchill, C. W., Drinkwater, M. J., & Barrow, J. D., 1999, Physical Review Letters, 82, 884
Webb, J. K., King, J. A., Murphy, M. T., Flambaum, V. V., Carswell, R. F., & Bainbridge, M. B., 2011, Physical Review Letters, 107, 191101
Wendt, M. & Molaro, P., 2011, A&A, 526, A96+
Whitmore, J. B., Murphy, M. T., & Griest, K., 2010, ApJ, 723, 89
Wolfe, A. M., Briggs, F. H., Turnshek, D. A., Davis, M. M., Smith, H. E., & Cohen, R. D., 1985, ApJ, 294, L67
Wolfe, A. M., Brown, R. L., & Roberts, M. S., 1976, Physical Review Letters, 37, 179
Zsargo, J. & Federman, S. R., 1998, ApJ, 498, 256

APPENDIX A: RESULTS OF CORRELATION ANALYSIS

Table A1. Shifts of individual spectra relative to the combined one in J0108−0037 at the position of different absorption profiles

species	EXP1 ($m\,s^{-1}$)	EXP2 ($m\,s^{-1}$)	EXP3 ($m\,s^{-1}$)	EXP4 ($m\,s^{-1}$)
(1)	(2)	(3)	(4)	
Ni II λ1454	656± 505	-826± 681	531± 458	-536± 463
Ni II λ1467	-131± 595	-1081± 835	-973± 764	484± 534
Ni II λ1502	-1094± 556	925± 887	62± 816	65± 941
Ni II λ1703	-391± 359	169± 473	1306± 778	161± 618
Ni II λ1709	-11± 184	230± 211	-408± 227	43± 195
Ni II λ1741	-145± 142	275± 164	-160± 171	-98± 162
Ni II λ1751	-496± 204	240± 221	165± 223	-152± 211
Cr II λ2056	-149± 109	109± 121	133± 135	-80± 121
Cr II λ2062	-83± 117	-168± 130	99± 139	151± 132
Cr II λ2066	-66± 162	15± 176	-267± 202	220± 179
Mn II λ2576	32± 102	115± 111	-44± 110	-123± 105
Mn II λ2594	-176± 133	-220± 151	181± 150	156± 142
Mn II λ2606	-187± 149	607± 173	-181± 168	-140± 165
Zn II λ2026	-207± 166	234± 188	-209± 194	170± 184
Zn II λ2062	-108± 166	79± 175	-267± 198	218± 182
Fe II λ1611	-282± 228	74± 290	752± 305	-373± 267
Fe II λ2249	-145± 103	80± 110	-118± 116	182± 118
Fe II λ2260	-358± 90	300± 100	-56± 105	183± 106
Si II λ1808	-237± 108	132± 127	239± 138	-50± 124
weighted mean	-171	+127	-14	+38
weighted standard deviation	152	207	223	166
weighted standard deviation of all exposures		134		

Table A2. Shifts of individual spectra relative to the combined one in J1623+0718 at the position of different absorption profiles

species	EXP1 ($m\,s^{-1}$)	EXP2 ($m\,s^{-1}$)	EXP3 ($m\,s^{-1}$)	EXP4 ($m\,s^{-1}$)
Ni II λ1454	2075± 573	-414± 582	94± 393	-840± 364
Ni II λ1703	2230±1013	-531± 682	378± 446	-414± 419
Ni II λ1709	-161± 465	520± 414	485± 499	-1040± 414
Cr II λ2062	177± 564	-180± 341	-191± 530	242± 274
Cr II λ2066	-434± 687	461± 633	335± 745	-684± 602
Zn II λ2062	-1434± 643	461± 633	72± 615	460± 408
Mn II λ2576	498± 426	0± 346	235± 420	-217± 224
Mn II λ2594	-46± 458	80± 303	572± 386	-185± 213
Mn II λ2606	475± 481	-1068± 735	-1073± 574	194± 283
Fe II λ1611	2002± 612	1394± 770	766±1559	-432± 335
Fe II λ2249	-555± 389	500± 273	-415± 424	-70± 305
Fe II λ2260	342± 320	635± 322	-632± 366	-164± 194
Fe II λ2374	-55± 184	678± 161	-913± 193	8± 110
Fe II λ2382	-275± 142	460± 139	-329± 160	25± 89
Fe II λ2586	196± 160	451± 139	-237± 158	-307± 87
Si II λ1808	142± 261	224± 220	414± 253	-381± 180
weighted mean	+44	+401	-233	-145
weighted standard deviation	543	314	480	251
weighted standard deviation of all exposures		313		

Table A3. Shifts of individual spectra relative to the combined one in J2340−0053 at the position of different absorption profiles

species	EXP1 ($m\,s^{-1}$)	EXP2 ($m\,s^{-1}$)	EXP3 ($m\,s^{-1}$)	EXP4 ($m\,s^{-1}$)	EXP5 ($m\,s^{-1}$)	EXP6 ($m\,s^{-1}$)	HIRES ($m\,s^{-1}$)
Ni II λ1709	-645± 358	212± 428	144± 336	759± 455	380± 412	74± 345	2530± 296
Ni II λ1741	-81± 380	5± 361	447± 296	668± 321	97± 282	-958± 317	626± 232
Ni II λ1751	-409± 513	-122± 392	588± 297	-180± 373	-406± 354	142± 332	65± 521
Cr II λ2056	-169± 759	303± 868	139± 761	-307± 922	263± 811	-41± 555	-43± 196
Cr II λ2062	-206± 749	184± 747	217± 574	49± 927	-213± 574	-467± 606	244± 268
Cr II λ2066	728±1026	-646±1201	233± 988	-561±1246	74±1179	-446±1042	—-
Zn II λ2026	155± 425	130± 486	-88± 377	-692± 389	205± 290	194± 325	—-
Mn II λ2576	-197± 351	219± 407	487± 400	-10± 384	-13± 368	-209± 290	—-
Mn II λ2594	-621± 375	129± 370	122± 384	-41± 363	476± 361	-110± 274	—-
Mn II λ2606	-143± 317	-439± 405	885± 310	-139± 361	436± 298	-1199± 284	—-
Fe II λ1608	-309± 66	117± 72	275± 62	-48± 81	113± 68	-205± 65	47± 48
Fe II λ1611	-15± 408	128± 385	66± 287	281± 493	-325± 532	-764± 456	2271± 539
Fe II λ2249	-103± 184	-104± 260	-221± 198	-307± 195	171± 183	138± 149	-433± 193
Fe II λ2260	-1272± 138	208± 133	110± 117	43± 136	594± 109	132± 101	-27± 21
Fe II λ2374	-308± 41	185± 41	230± 37	35± 40	315± 35	-294± 32	148± 57
Si II λ1808	-380± 139	-137± 160	357± 144	122± 154	249± 157	-165± 134	-229± 92
weighted mean	-352	146	236	18	283	-238	110
weighted standard deviation	296	127	148	173	184	238	438
weighted standard deviation of all exposures			204*				

$\star$standard deviation in HIRES column is not included in the averaged standard deviation.

Table A4. Shifts of individual spectra relative to the combined one in J2358−1020 at the position of different absorption profiles

species	EXP1 ($m\,s^{-1}$)	EXP2 ($m\,s^{-1}$)	EXP3 ($m\,s^{-1}$)	EXP4 ($m\,s^{-1}$)	EXP5 ($m\,s^{-1}$)	EXP6 ($m\,s^{-1}$)	EXP7 ($m\,s^{-1}$)
Zn II λ2026	-509± 549	-477± 376	-744± 629	1083± 395	173± 266	165± 326	-511± 553
Mn II λ2576	-555± 521	73± 419	-658± 420	-488± 406	150± 317	322± 413	1316± 578
Fe II λ2249	-13± 747	-317±1013	-370± 596	-203± 452	753± 730	397± 456	-568± 473
Fe II λ2344	-19± 234	88± 251	-257± 247	-311± 189	32± 151	290± 201	72± 201
Fe II λ2374	-800± 294	- 118± 213	-35± 261	10± 177	205± 156	188± 174	392± 264
Fe II λ2586	-130± 268	331± 243	24± 245	-213± 166	139± 165	258± 180	-178± 246
Si II λ1808	-20± 577	-619± 661	-1897± 719	-497± 499	241± 421	612± 527	1975± 768
weighted mean	-275	+70	-242	-129	+142	+147	+111
weighted standard deviation	357	288	431	374	113	260	561
weighted standard deviation of all exposures			170				